Stochastic modeling of discontinuous dynamic recrystallization at finite strains in hcp metals

A.D. Tutcuoglu, A. Vidyasagar, K. Bhattacharya, D.M. Kochmann

PII: S0022-5096(18)30356-9
DOI: https://doi.org/10.1016/j.jmps.2018.09.032
Reference: MPS 3463

To appear in: *Journal of the Mechanics and Physics of Solids*

Received date: 30 April 2018
Revised date: 29 August 2018
Accepted date: 25 September 2018

Please cite this article as: A.D. Tutcuoglu, A. Vidyasagar, K. Bhattacharya, D.M. Kochmann, Stochastic modeling of discontinuous dynamic recrystallization at finite strains in hcp metals, *Journal of the Mechanics and Physics of Solids* (2018), doi: https://doi.org/10.1016/j.jmps.2018.09.032

Stochastic modeling of discontinuous dynamic recrystallization at finite strains in hcp metals

A. D. Tutcuoglu[a,b], A. Vidyasagar[a,b], K. Bhattacharya[b], D. M. Kochmann[a,b,*]

[a] *Mechanics & Materials, Department of Mechanical and Process Engineering, ETH Zürich, 8092 Zürich, Switzerland*
[b] *Division of Engineering and Applied Science, California Institute of Technology, CA 91125 Pasadena, USA*

Abstract

We present a model that aims to describe the effective, macroscale material response as well as the underlying mesoscale processes during discontinuous dynamic recrystallization under severe plastic deformation. Broadly, the model brings together two well-established but distinct approaches – first, a continuum crystal plasticity and twinning approach to describe complex deformation in the various grains, and second, a discrete Monte-Carlo-Potts approach to describe grain boundary migration and nucleation. The model is implemented within a finite-strain Fast Fourier Transform-based framework that allows for efficient simulations of recrystallization at high spatial resolution, while the grid-based Fourier treatment lends itself naturally to the Monte-Carlo approach. The model is applied to pure magnesium as a representative hexagonal closed packed metal, but is sufficiently general to admit extension to other material systems. Results demonstrate the evolution of the grain architecture in representative volume elements and the associated stress–strain history during the severe simple shear deformation typical of equal channel angular extrusion. We confirm that the recrystallization kinetics converge with increasing grid resolution and that the resulting model captures the experimentally observed transition from single- to multi-peak stress–strain behavior as a function of temperature and rate.

Keywords: Recrystallization, Monte-Carlo, Homogenization, Magnesium, Polycrystal

1. Introduction

Strengthening metals through grain refinement based on the relation of Hall (1951) and Petch (1953) can be achieved by a number of forming processes that induce a microstructural reorganization of the polycrystalline grain structure, with processes ranging from asymmetric roll bonding and asymmetric rolling to high-pressure torsion and equal channel angular extrusion (ECAE) (see e.g. Hallberg (2011); Sakai et al. (2014)). Controlling a material's performance through such processing routes calls for accurate structure–property relations as well as for efficient computational models that predict the underlying microstructural mechanisms as a function of the thermo-mechanical process parameters. Here, we present a micromechanical model which describes recrystallization, one of the key underlying causal mechanisms of changes to the grain structure in metals, encountered e.g. during the ECAE process.

Recrystallization occurs in various ways. *Static recrystallization* is a temperature-driven process that occurs under slowly-varying, creep-like loading conditions such as during annealing (Sakai et al., 2014; Zhang et al., 2013), where the average grain size increases with a negative impact on the strength properties. This can be overcome, e.g., through alloying by rare earth metals, as shown for Mg-Zn-Zr alloys enriched with Er and undergoing static recrystallization at high temperatures (Zhang et al., 2013). Occurring at higher loading rates, *dynamic recrystallization*[1] emerges from the competition between recrystallization and continued plastic deformation such as during ECAE. It is further

*Phone +41-44-632-32-76.
Email address: dmk@ethz.ch (D. M. Kochmann)

[1] Note that *dynamic* refers to the fact that the recrystallization mechanisms occur during continued plastic deformation. It does not refer to inertia or shocks.

subcategorized according to the two underlying microstructural processes. Generally observed in high-stacking-fault-energy metals such as aluminum, *continuous dynamic recrystallization* describes the gradual transformation of subgrain structures formed from dislocation networks into new grains, resulting in grain refinement (Tan and Tan, 2003; Gourdet and Montheillet, 2003; Bacca et al., 2015). *Discontinuous dynamic recrystallization* describes the process of grain nucleation at high-energy sites and the subsequent grain growth by grain boundary migration (Fatemi-Varzaneh et al., 2007, 2013; Cram et al., 2009), which predominantly occurs in metals with low stacking fault energy such as magnesium (Mg) (Sakai et al., 2014). While it is generally acknowledged that nucleation is driven by the reduction of stored elastic and plastic strain energy density (Sreekala and Haataja, 2007; Totten et al., 2004), the exact nucleation criterion is a debated subject: a critical local dislocation density required for nucleation is frequently proposed (Takaki et al., 2008; Sakai et al., 2014), whereas other reports concentrate on a critical (plastic) strain instead (Cram et al., 2009; Chen et al., 2015); yet another approach is based on a critical inelastic strain energy density Mellbin et al. (2016). As a competing mechanism, grain boundary migration, is driven by the difference in stored strain energy between neighboring grains with differing plastic histories (Hallberg, 2011; Huang and Logé, 2016). Thus, discontinuous dynamic recrystallization involves the interplay between three phenomena – severe plastic deformation of a polycrystal, grain boundary migration and grain nucleation. In particular the interplay of classical continuum plasticity deformation modes with the statistical nature of grain nucleation and boundary motion poses modeling challenges, which is the focus of this paper.

Numerous models have been established to model dynamic recrystallization. Among the most prominent ones stands the *phase-field method*, in which every grain is associated with a continuous order parameter defined throughout a representative volume element (RVE) (Chen et al., 2015; Sreekala and Haataja, 2007; Moelans et al., 2013). While grain boundary migration is naturally integrated into such a diffuse-interface description through, e.g., Allen-Cahn-type kinetics for the order parameter (Allen and Cahn, 1972), modeling grain nucleation is not as readily accomplished. For example, Chen et al. (2015) nucleated grains in the framework of static recrystallization with new grains exclusively deforming in an elastic manner, hence allowing for comparison with phenomenological recrystallization theories such as the JMAK model of Kolmogorov (1937); Johnson and Mehl (1939); Avrami (1939), but preventing the typical multi-peak stress–strain behavior observed during discontinuous dynamic recrystallization. Similarly, Zhao et al. (2016, 2018) presented a scheme coupling FFT-based viscoelastic and phase-field models in conjunction with an elaborate statistics-based nucleation criterion to capture dynamic recrystallization in copper. Although their model successfully replicates the single-peak stress–strain evolution in a compression experiment involving dynamic recrystallization at 723 K, it is restricted to linearized kinematics without strong plastic anisotropy. Furthermore, the fully recrystallized state assumes no contribution to the stored energy, so that multi-peak stress–strain behavior is out of the scope in that scheme. Gentry and Thornton (2015) investigated recrystallization in titanium, a metal which possesses hexagonal close-packed (hcp) crystallography at room temperature. Their model, however, does not capture twinning and – similar to Chen et al. (2015) – nucleation is introduced in a simplified, numerically convenient way (new grains are introduced as spherical, dislocation-free regions held constant for a period of time to prevent the interface energy from forcing the recrystallized grain to disappear). Although phase-field models are highly parallelizable, tracking the evolution of every order parameter nevertheless demands for extensive computational resources (which can be mitigated somewhat by tracking the support of each order parameter (Takaki et al., 2008; Kim et al., 2006)).

Computationally less expensive alternatives are discrete state methods such as *cellular automata* and the *Monte-Carlo-Potts* (MCP) model. Various such models have been proposed for recrystallization but have been limited by their simplifying constitutive or kinematic assumptions. Ding and Guo (2001) and Hallberg et al. (2010), e.g., presented cellular automata to model discontinuous dynamic recrystallization in copper. While the nucleation rate in their models did depend on strain rate and temperature (allowing the model to replicate their respective influence on single- and multiple-peak stress–strain responses), the underlying plasticity model (based on Mecking and Kocks (1981), using the dislocation density as the sole internal variable) is insufficient in cases of severe plastic anisotropy.

As an alternative discrete state method, Rollett et al. (1992) introduced an MCP model to capture the strain rate- and temperature-dependent transition from single- to multi-peak flow in order to analyze the importance of the initial average grain size; yet the underlying plasticity model was relatively simple and insufficient for hcp metals. A 3D-Monte-Carlo model was presented by Ivasishin et al. (2006), which introduced the influence of surface tension via shape factors and included misorientation dependence of the grain boundary energy through the model of Read and Shockley (1950). An overview over the aforementioned models as well as alternatives such as the *level set method* and *vortex method* is provided by the reviews of Hallberg (2011) and Huang and Logé (2016).

In addition to the shortcomings of prior models of recrystallization, the majority of the above presented models is restricted to metals experiencing isotropic inelasticity. As a consequence, those models do not apply to hexagonal closed packed (hcp) metals such as Mg and its alloys, experiencing anisotropic plasticity as well as alternative strain-accommodating processes such as deformation twinning (Christian and Mahajan, 1995) whose finite twinning shears are not representable by small-strain models. Recent work by Asadi et al. (2015) captured dynamic recovery and dynamic recrystallization in Mg alloy AZ91 by a 2D cellular automaton. However, the underlying material model based on Mecking and Kocks (1981) does not yield an accurate representation of the anisotropic inelasticity in hcp metals. Furthermore, homogeneity within grains was assumed. Still based on the assumption that flow stress is dependent on a single scalar variable, Wang et al. (2018) used the model of Estrin and Mecking (1984) within a 2D cellular automaton to model dynamic recrystallization in Mg alloy ZM21; however, that model neglected linear momentum conservation on the microscale and hence did not capture the heterogeneous deformation within grains.

While all of the above approaches have provided insight into particular aspects of dynamic recrystallization, a comprehensive model that captures discontinuous dynamic recrystallization at finite deformations, while accounting for the statistical nature of grain nucleation and migration, and suitable for strong inelastic anisotropy is presently missing – but needed to understand, e.g., ECAE of Mg alloys. The goal of this paper is to fill this gap. The key idea is illustrated in Figure 1. We perform fully resolved simulations of the plastic deformation in polycrystals using an extended crystal plasticity model in conjunction with a Fast-Fourier-transform (FFT) based solver. The fully resolved simulation allows us to capture the non-uniformity of plastic deformation at the subgranular level and appropriately mimics the deterministic nature at the time-scale of interest. Simultaneously, we model grain boundary migration and grain nucleation using a statistical MCP model. Since the latter requires a discrete regular grid, we use the FFT-based continuum mechanics solver to blend the continuum and discrete approaches. Each grid point is associated with a particular grain and carries information about the crystallographic orientation as well as elastic and plastic states. At each Monte-Carlo time step, we either migrate the grain boundary or nucleate a new grain based on probabilities that depend on the elastic and plastic states of the grid point. We subsequently update the elastic and plastic states and iterate. For the time scale of interest, this allows us to couple the deterministic nature of plastic deformation with the stochastic nature of grain nucleation and migration. Representative of the highly anisotropic inelastic deformation mechanisms in hcp metals, we choose an extended crystal plasticity model for pure Mg Chang and Kochmann (2015); Chang et al. (2017), which includes twinning in an effective, volume-fraction based sense.

The remainder of this contribution is structured as follows. Section 2 briefly summarizes the constitutive model for Mg as a representative hcp material and the FFT-based homogenization scheme which turns the continuum RVE problem into a discrete grid-based problem. Within this framework, Section 3 introduces the model for recrystallization, followed by a verification of proper convergence and scaling of the numerical scheme in Section 4. Once the theory has been laid out and the numerics verified, simulations of the microstructural evolution and resulting effective response of Mg during ECAE are presented in Section 5. To demonstrate the versatility of the model, the influence of its various parameters on the material response is illustrated in Section 6. Finally, Sections 7 and 8 discuss the findings and conclude our investigation, respectively.

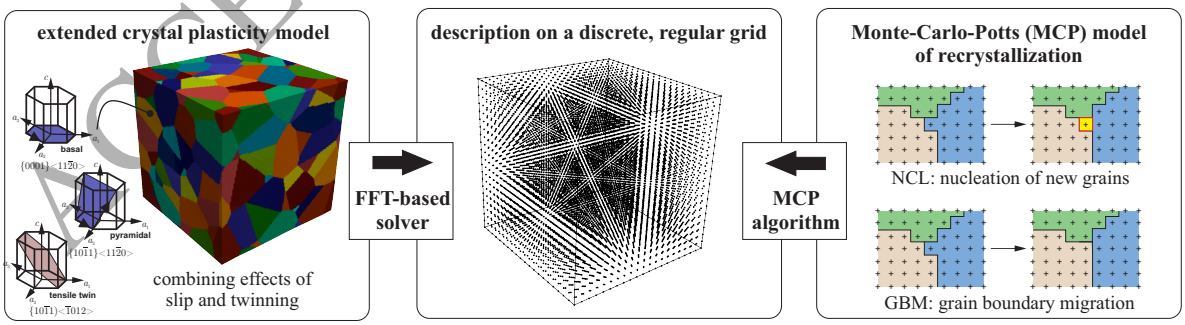

Figure 1: Schematic overview of the presented model, which uses an extended crystal plasticity formulation whose FFT-based discrete solution allows for the coupling to a Monte-Carlo-Potts description of recrystallization.

2. RVE-level finite-strain crystal plasticity continuum model and discretization

2.1. *Single-crystal constitutive model: slip & twinning in magnesium*

Plasticity in hcp metals emerges from the activation of a total of $n_s = 18$ slip systems: ⟨c+a⟩-pyramidal and ⟨a⟩-pyramidal systems each contribute six systems, alongside basal and prismatic slip which each contribute three slip systems. The significantly lower critical resolved shear stresses in the basal plane as compared to slip on non-basal planes results in the activation of alternative strain-accommodating processes, which in the case of hcp metals is provided by deformation twinning (Christian and Mahajan, 1995). Although recent studies based on density functional theory (DFT) suggest the presence of eleven twin systems (Sun et al., 2017), we here constrain ourselves to the two most easily activated systems, viz. compression and extension twins (with the respective names referring to the loading along the *c*-axis). Also, we restrict our model to the inclusion of the basal, prismatic and ⟨c+a⟩-pyramidal systems, while neglecting ⟨a⟩-pyramidal systems based on the discussion in Chang and Kochmann (2015). Plastic slip is quantified through the notion of *slip activities* $\boldsymbol{\gamma} = \{\gamma_1, \dots, \gamma_{n_2}\} \in \mathbb{R}^{n_s}$. To capture hardening, we define the accumulated plastic slips $\boldsymbol{\varepsilon} = \{\varepsilon_1, \dots, \varepsilon_{n_2}\} \in \mathbb{R}^{n_s}_+$ via the evolution law (with initial condition $\boldsymbol{\varepsilon} = \boldsymbol{0}$)

$$\dot{\epsilon}_\alpha = |\dot{\gamma}_\alpha| \qquad \forall \quad \alpha \in \{1, ..., n_s\}. \tag{1}$$

Since twin lamellae may form on length scales far below the granular scale, we follow the strategy of (Agnew et al., 2001; Staroselsky and Anand, 2003; Graff et al., 2007; Homayonifar and Mosler, 2011; Zhang and Joshi, 2012) and define the homogenized notion of a *twin volume fraction* $\boldsymbol{\lambda} = \{\lambda_1, \dots, \lambda_{n_{\text{tw}}}\} \in [0,1]^{n_{\text{tw}}}$, capturing the local effective volume fraction[2] of the twinned crystal at any point on the polycrystalline mesoscale, where n_{tw} denotes the number of twin systems. We further impose the constraint $\sum_{\beta=1}^{n_{\text{tw}}} \lambda_\beta \leq 1$.

Following Kalidindi (2001), we neglect the effect of kinematic interactions between slip and twinning but instead include relaxation due to both slip and twinning into $\boldsymbol{F}^{\text{in}}$ so as to yield the multiplicative decomposition $\boldsymbol{F} = \boldsymbol{F}^{\text{e}}\boldsymbol{F}^{\text{in}}$ with $\boldsymbol{F} = \text{Grad}\,\boldsymbol{\varphi}$ denoting the deformation gradient. The additive decomposition of the velocity gradient,

$$\boldsymbol{l} = \dot{\boldsymbol{F}}\boldsymbol{F}^{-1} = \boldsymbol{l}^{\text{e}} + \boldsymbol{l}^{\text{in}} = \boldsymbol{l}^{\text{e}} + \boldsymbol{F}^{\text{e}}\tilde{\boldsymbol{l}}^{\text{in}}(\boldsymbol{F}^{\text{e}})^{-1} \qquad \text{with} \qquad \boldsymbol{l}^{\text{e}} = \dot{\boldsymbol{F}}^{\text{e}}(\boldsymbol{F}^{\text{e}})^{-1}, \quad \tilde{\boldsymbol{l}}^{\text{in}} = \dot{\boldsymbol{F}}^{\text{in}}(\boldsymbol{F}^{\text{in}})^{-1}, \tag{2}$$

introduces the effects of slip and twinning via the inelastic velocity gradient (Chang and Kochmann, 2015)

$$\tilde{\boldsymbol{l}}^{\text{in}} = \tilde{\boldsymbol{l}}^{\text{p}} + \tilde{\boldsymbol{l}}^{\text{tw}} \qquad \text{with} \qquad \begin{cases} \tilde{\boldsymbol{l}}^{\text{p}} = \sum_{\alpha=1}^{n_{\text{s}}} \dot{\gamma}_\alpha \underbrace{\left[\left(1 - \sum_{\beta=1}^{n_{\text{tw}}} \lambda_\beta\right)\boldsymbol{s}_\alpha \otimes \boldsymbol{m}_\alpha + \sum_{\beta=1}^{n_{\text{tw}}} \lambda_\beta \boldsymbol{s}'_{\alpha\beta} \otimes \boldsymbol{m}'_{\alpha\beta}\right]}_{\equiv \boldsymbol{p}_\alpha}, \\ \tilde{\boldsymbol{l}}^{\text{tw}} = \sum_{\beta=1}^{n_{\text{tw}}} \dot{\lambda}_\beta \gamma^{\text{tw}}_\beta \boldsymbol{a}_\beta \otimes \boldsymbol{n}_\beta. \end{cases} \tag{3}$$

Here, vectors $(\boldsymbol{s}_\alpha, \boldsymbol{m}_\alpha)$ define slip system α, whereas $(\boldsymbol{a}_\beta, \boldsymbol{n}_\beta)$ define twin system β and γ^{tw}_β denotes the respective twinning strain. The two mirrored slip systems in the twinned crystal result from a Householder mapping applied to the respective parent slip system such that

$$\boldsymbol{s}'_{\alpha\beta} = \boldsymbol{Q}_\beta \boldsymbol{s}_\alpha, \quad \boldsymbol{m}'_{\alpha\beta} = \boldsymbol{Q}_\beta \boldsymbol{m}_\alpha, \quad \boldsymbol{Q}_\beta = \boldsymbol{I} - 2\boldsymbol{n}_\beta \otimes \boldsymbol{n}_\beta. \tag{4}$$

We use a variational setting based on the Helmholtz free energy density $W = W(\boldsymbol{F}, \boldsymbol{F}^{\text{in}}, \boldsymbol{\varepsilon}, \boldsymbol{\lambda})$ which decomposes into elastic strain energy and plastic stored energy due to slip and twinning according to

$$W(\boldsymbol{F}, \boldsymbol{F}^{\text{in}}, \boldsymbol{\varepsilon}, \boldsymbol{\lambda}) = W_{\text{el}}\left(\boldsymbol{F}\left(\boldsymbol{F}^{\text{in}}\right)^{-1}\right) + W_{\text{sl}}(\boldsymbol{\varepsilon}) + W_{\text{tw}}(\boldsymbol{\lambda}). \tag{5}$$

[2] The *effective* twin volume fractions $\lambda_\beta \in [0,1]$ capture only the effects of crystallographic reorientations at the relevant mesoscopic scale in a homogenized sense (by reorienting the slip and twin systems), without describing individual twin lamellae at lower scales. This model thus captures stress concentrations at twin boundaries only in case of macro-twins on the level of the numerical discretization (and analogous to GBs) while local concentrations near, e.g., nanoscale twin lamellae are not accounted for explicitly.

We further define the dual dissipation potential (Ortiz and Repetto, 1999) as

$$\Psi^*(\dot{\boldsymbol{\varepsilon}}, \dot{\boldsymbol{\lambda}}) = \Psi^*_{\mathrm{sl}}(\dot{\boldsymbol{\varepsilon}}) + \Psi^*_{\mathrm{tw}}(\dot{\boldsymbol{\lambda}}), \tag{6}$$

so that the principle of the minimum dissipation potential yields differential inclusions of the form

$$\begin{cases} 0 \in \dfrac{\partial}{\partial \dot{\gamma}_\alpha}\left(\dot{W} + \Psi^*\right) = -|\tau^{\mathrm{p}}_\alpha| + \dfrac{\partial W_{\mathrm{sl}}}{\partial \epsilon_\alpha} + \dfrac{\partial \Psi^*_{\mathrm{sl}}}{\partial \dot{\epsilon}_\alpha} & \forall \quad \alpha \in \{1, \dots, n_{\mathrm{s}}\} \\ 0 \in \dfrac{\partial}{\partial \dot{\lambda}_\beta}\left(\dot{W} + \Psi^*\right) = -\tau^{\mathrm{tw}}_\beta + \dfrac{\partial W_{\mathrm{tw}}}{\partial \lambda_\beta} + \dfrac{\partial \Psi^*_{\mathrm{tw}}}{\partial \dot{\lambda}_\beta} & \forall \quad \beta \in \{1, \dots, n_{\mathrm{tw}}\} \end{cases} \quad \text{with} \quad \begin{cases} \tau^{\mathrm{p}}_\alpha = \boldsymbol{\Sigma} \cdot \boldsymbol{p}_\alpha \\ \tau^{\mathrm{tw}}_\beta = \gamma^{\mathrm{tw}}_\beta \boldsymbol{\Sigma} \cdot \left(\boldsymbol{a}_\beta \otimes \boldsymbol{n}_\beta\right) \end{cases}, \tag{7}$$

where $\boldsymbol{\Sigma} = (\boldsymbol{F}^{\mathrm{e}})^{\mathrm{T}} \boldsymbol{P} (\boldsymbol{F}^{\mathrm{in}})^{\mathrm{T}}$ denotes the Mandel stress tensor, and $\boldsymbol{P} = \partial W / \partial \boldsymbol{F} = \partial W_{\mathrm{el}} / \partial \boldsymbol{F}$ represents the first Piola Kirchhoff stress tensor.

The elastic strain energy density is modeled using the isotropic compressible Neo-Hookean energy density

$$W_{\mathrm{el}}(\boldsymbol{F}) = \frac{\mu}{2}\left(\frac{I_1}{J^{-2/3}} - 3\right) + \frac{\lambda}{2}(J-1)^2 \qquad \text{with} \qquad I_1 = \mathrm{tr}\left(\boldsymbol{F}^T \boldsymbol{F}\right), \quad J = \det \boldsymbol{F} \tag{8}$$

with μ and λ denoting the shear and bulk modulus, respectively. The choice of an isotropic model is based on the work of Chang and Kochmann (2015) who showed that anisotropic elastic models (see, e.g., Schröder et al. (2008)) have negligible effects on simulated results – due to the low elastic anisotropy in Mg – while increasing computational costs.

The inelastic strain energy density due to slip is decomposed into self- and latent hardening contributions and adds to the plastic anisotropy inherent in hcp metals:

$$W_{\mathrm{sl}} = W_{\mathrm{sl,lat}} + W_{\mathrm{sl,self}} = \frac{1}{2}\boldsymbol{\varepsilon} \cdot \mathcal{H}\boldsymbol{\varepsilon} + \sum_\alpha \sigma^\infty_\alpha \left[\epsilon_\alpha + \frac{\sigma^\infty_\alpha}{h_\alpha} \exp\left(-\frac{h_\alpha \epsilon_\alpha}{\sigma^\infty_\alpha}\right)\right], \tag{9}$$

where Voce hardening (Agnew et al., 2001; Graff et al., 2007) captures the high resistance of prismatic and pyramidal slip (Homayonifar and Mosler, 2011) with σ^∞_α and h_α representing the ultimate stress and hardening rate on the α^{th} slip system, respectively. $\mathcal{H}$ is a symmetric matrix endowed with the hardening moduli on its off-diagonals and a zero diagonal (which is positive-definite for all sensible values of ϵ_α). For twinning, we assume quadratic hardening for both self-induced as well as latent twin hardening, with self-hardening moduli h_β and zero-diagonal endowed, symmetric latent hardening matrix $\mathcal{K}$, yielding

$$W_{\mathrm{tw}} = W_{\mathrm{tw,self}} + W_{\mathrm{tw,lat}} \quad \text{with} \quad \begin{cases} W_{\mathrm{tw,self}} = \displaystyle\sum_{\beta=1}^{n_{\mathrm{tw}}} \frac{1}{2} h_\beta \lambda_\beta^2 \\ W_{\mathrm{tw,lat}} = \dfrac{1}{2}\boldsymbol{\lambda} \cdot \mathcal{K}\boldsymbol{\lambda} \end{cases}. \tag{10}$$

Following Ortiz and Stainier (1999), power-law dissipation potentials of the form

$$\Psi^*_{\mathrm{sl}}(\dot{\boldsymbol{\gamma}}) = \sum_{\alpha=1}^{n_{\mathrm{tw}}} \frac{\tau_{0,\alpha}\dot{\gamma}_{0,\alpha}}{m_\alpha + 1}\left(\frac{\dot{\gamma}_\alpha}{\dot{\gamma}_{0,\alpha}}\right)^{m_\alpha + 1} \qquad \text{and} \qquad \Psi^*_{\mathrm{tw}} = \sum_{\beta=1}^{n_{\mathrm{tw}}} \frac{\tau_{0,tw,\beta}\dot{\lambda}_{0,\beta}}{m_{\mathrm{tw},\beta} + 1}\left(\frac{\dot{\lambda}_\beta}{\dot{\lambda}_{0,\beta}}\right)^{m_{\mathrm{tw},\beta}+1}, \tag{11}$$

are introduced for plastic slip and twinning, respectively. The slip hardening exponent m_α is close to 0 to approximate rate independence without compromising the ability to explicitly perform internal variable updates. Although recent findings suggest rate independence for twinning (Ulacia et al., 2010), in the framework of explicit state updates, we follow Chang and Kochmann (2015) and choose the above dissipation potential where $m_{tw,\beta}$, $\tau_{0,tw,\beta}$ and $\dot{\lambda}_{0,\beta}$ represent the twin hardening exponent, critical resolved shear stress, and reference twin rate for the β^{th} twin system, respectively.

Even though implicit variational constitutive updates (Ortiz and Stainier, 1999) allow for significantly larger load/time steps as shown by Chang and Kochmann (2015) for the present constitutive model, we here favor explicit updates for the following reasons. Explicit updates improve numerical stability and convergence for high numbers of

slip and twin systems as those described here. Also, recrystallization (discussed in Section 3) will be treated in an explicit fashion and, at times, requires to be resolved at time steps smaller than those characteristic of implicit updates. Therefore, we solve the evolution laws for both slip and twin ratios explicitly,

$$\dot{\gamma}_\alpha = \dot{\gamma}_{0,\alpha} \left| \frac{|\tau_\alpha^{\mathrm{p}}| - \frac{\partial W^{\mathrm{p}}}{\partial \epsilon_\alpha}}{\tau_{0,\alpha}} \right|^{1/m_\alpha} \mathrm{sign}\left(\tau_\alpha^{\mathrm{p}}\right) \qquad \text{and} \qquad \dot{\lambda}_\beta = \dot{\lambda}_{0,\beta} \left| \frac{\tau_\beta^{\mathrm{p}} - \frac{\partial W^{\mathrm{p}}}{\partial \lambda_\beta}}{\tau_{0,\beta}} \right|^{1/m_{\beta,\mathrm{tw}}}, \tag{12}$$

by explicit time integration using a forward-Euler scheme, provided $m_\alpha, m_{\beta,\mathrm{tw}} \neq 0$. Since the nearly rate independence demands small hardening coefficients $m_{\alpha,\mathrm{p}}$, small increments are required to prevent the forward-Euler scheme from overshooting. All numerical values of the model parameters are summarized in Table A.2.

2.2. *Polycrystal response and FFT-based homogenization*

The above crystal plasticity model is employed within an RVE Ω that contains a representative grain network at the mesoscale. Mechanical equilibrium is enforced with periodic boundary conditions on its boundary $\partial\Omega$ in order to link the microstructural fields to the effective material behavior at the macroscale, as observed in metal forming processes. To this end, we follow concepts of classical homogenization (Kouznetsova et al., 2001; Miehe et al., 2002; Geers et al., 2010) where the the macroscopic deformation gradient $\boldsymbol{F}^*$ is imposed as the RVE average, i.e., $\langle \boldsymbol{F}(\boldsymbol{X}) \rangle = \boldsymbol{F}^*$ where $\langle \cdot \rangle = |\Omega|^{-1} \int_\Omega (\cdot) \mathrm{d}V$. Within the RVE, the deformation mapping is obtained from quasistatic linear momentum balance, $\mathrm{Div}\, \boldsymbol{P} = \boldsymbol{0}$, while the internal variables follow the inelastic evolution laws discussed above. The macroscopically experienced, effective stress equals the RVE average $\boldsymbol{P}^* = \langle \boldsymbol{P}^*(\boldsymbol{X}) \rangle$. In the chosen applications we neglect body forces and inertial effects.

With the MCP model in mind, we discretize the RVE into a regular grid and apply the concepts of Moulinec and Suquet (1994) to solve the governing equations in Fourier space (see also Lebensohn et al. (2012); Eisenlohr et al. (2013); Lebensohn and Needleman (2016)). To this end, the RVE is discretized into $n = N^3$ grid points in 3D space, with N denoting the number of grid points per side and $\boldsymbol{X}^k, k \in \{1, ..., n\}$ referring to the position of each grid point in the undeformed configuration.

Our numerical predictor-corrector iterative scheme starts with an initial guess $\boldsymbol{F}^0(\boldsymbol{X}^k)$ for the distribution of $\boldsymbol{F}(\boldsymbol{X}^k)$ in the RVE, which allows to evaluate the stress tensor field $\boldsymbol{P}^0(\boldsymbol{X}^k) = \boldsymbol{P}(\boldsymbol{F}^0(\boldsymbol{X}^k))$ as well as the stiffness tensor field $\mathbb{C}^0 = \mathbb{C}(\boldsymbol{F}^0(\boldsymbol{X}^k))$. We compute the average stiffness tensor $\mathbb{C}^{\mathrm{avg,m}} \equiv \langle \mathbb{C}^{\mathrm{m}}(\boldsymbol{X}) \rangle$ at each iteration step m by averaging over all grid points in the RVE. Based on the average stiffness tensor as a linear reference medium[3], we define a stress perturbation field $\boldsymbol{\tau}(\boldsymbol{X})$ such that at every point $\boldsymbol{X} \in \Omega$

$$\boldsymbol{\tau}^m(\boldsymbol{X}) = \boldsymbol{P}^m(\boldsymbol{X}) - \mathbb{C}^{\mathrm{avg},m} \boldsymbol{F}^m(\boldsymbol{X}), \tag{13}$$

Substituting (13) into the linear momentum conservation equation yields

$$\mathrm{Div}\, \boldsymbol{\tau}^m(\boldsymbol{X}) + \mathrm{Div}\left[\mathbb{C}^{\mathrm{avg},m} \boldsymbol{F}^m(\boldsymbol{X})\right] = \boldsymbol{0}. \tag{14}$$

Applying a discrete Fourier transform to (14) along with the relation $\boldsymbol{F}(\boldsymbol{X}) = \mathrm{Grad}\, \boldsymbol{\varphi}(\boldsymbol{X})$ yields an explicit update rule for the deformation gradient in Fourier space (with $\boldsymbol{K}^k \in \mathcal{T}$ denoting the wave vectors and $\mathcal{T}$ the complete set of the n wave vectors in Fourier space), which becomes, using indicial notation,

$$\hat{F}_{jL}^{m+1}(\boldsymbol{K}^k) = \begin{cases} \left[A_{ij}^m(\boldsymbol{K}^k)\right]^{-1} \hat{\tau}_{iJ}^m(\boldsymbol{K}^k) K_J^k K_L^k & \text{for } \boldsymbol{K}^k \neq \boldsymbol{0}, \\ F_{jL}^* & \text{for } \boldsymbol{K}^k = \boldsymbol{0}, \end{cases} \tag{15}$$

with the acoustic tensor components

$$A_{ik}^m(\boldsymbol{K}^k) = \mathbb{C}_{iJkL}^{\mathrm{avg},m} K_L^k K_J^k. \tag{16}$$

[3] Although it was shown that choosing the average stiffness tensor as a reference may lead to divergence, using $\mathbb{C}^{\mathrm{avg}}$ leads to stable results in our framework, thus avoiding the need for a more elaborated scheme as presented, e.g., by Kabel et al. (2014).

Starting with $\boldsymbol{F}^0(\boldsymbol{X}^k)$, this provides an iterative update procedure that is solved by fixed-point iteration: $\hat{\boldsymbol{F}}^{m+1}(\boldsymbol{K}^k)$ is computed in Fourier space, transformed into $\boldsymbol{F}^{m+1}(\boldsymbol{X}^k)$ in real space, followed by the evaluation of $\boldsymbol{P}^{m+1}(\boldsymbol{X}^k)$, $\boldsymbol{\tau}^{m+1}(\boldsymbol{X}^k)$ and $\mathbb{C}^{\text{ave},m+1}$. After Fourier transform, the resulting $\hat{\boldsymbol{P}}^{m+1}(\boldsymbol{K}^k)$ and $\hat{\boldsymbol{\tau}}^{m+1}(\boldsymbol{K}^k)$ are used in Fourier space for the next update, until convergence is achieved in the sense of the discrete L_2-norm of the stress perturbation $\boldsymbol{\tau}^m$.

Rather than applying the above FFT-based scheme directly, we use a finite-difference approximation for all spatial derivatives before applying the Fourier transform (Müller, 1998; Lebensohn and Needleman, 2016). This approximation, applied to the related problem of small-strain inelasticity in (Vidyasagar et al., 2017), uses a central-difference approximation and leads to the approximate Fourier transform of a derivative

$$\mathcal{F}\left(\frac{\partial f}{\partial x_i}\right) = -ihk_i\mathcal{F}(f) \approx -\frac{i\sin(hk_i\Delta x)}{\Delta x}\mathcal{F}(f), \tag{17}$$

which converges to the exact derivative with decreasing grid size ($\Delta x \to 0$). A major improvement, this finite-difference correction considerably mitigates ringing artifacts and Gibbs phenomena associated with sharp gradients in material properties (such as those across grain or twin boundaries). In Vidyasagar et al. (2017) and Vidyasagar et al. (2018), this correction was successfully applied to polycrystals of small-strain ferroelectric ceramics and of finite-strain crystal plasticity in Mg, respectively; the reader is referred to those publications for further information.

The above numerical scheme is solved in a time-incremental fashion to find a sequence of mechanical equilibria, using a constant time step Δt such that, here and in the following, $(\cdot)_\alpha$ denotes[4] a quantity evaluated at time $t_\alpha = \alpha \cdot \Delta t$.

3. A stochastic model for recrystallization

Modeling recrystallization requires to account for both grain nucleation (NCL) and migration (GBM), which is accomplished here by a stochastic model. In a nutshell, each point inside the RVE is associated with a particular grain through its crystallographic orientation (manifesting in the model through the slip and twin system orientations, and potentially through elastic anisotropy). The grain association of a material point is referred to as a its *state*. Consider an RVE containing n_G grains, so that each point has a unique integer state $s \in [1, n_G]$ describing its crystallographic orientation (in the undeformed configuration). At any point in time, a material point is allowed to undergo a *state switch*, i.e., to either nucleate a new grain (with a fresh crystallographic orientation, raising n_G by one) or, if in the vicinity of a grain boundary (GB), to join a neighboring grain and adopt its orientation. Whether or not such a state switch occurs depends on the current state of the local elastic and inelastic fields as well as on temperature and deformation history. Inspired by the Monte-Carlo-Potts (MCP) model (Potts, 1952) as well as the Monte-Carlo-Metropolis and Metropolis-Hasting algorithms (Metropolis et al., 1953; Molkaraie and Gómez, 2015), the probability of switching increases with the stored energy release upon a state switch. The probability also increases with temperature through thermal fluctuations. We exploit the the crystal plasticity framework introduced in Section 2 to define state switches and the related release of elastic and inelastic energy, and we exploit the FFT-based grid discretization to apply the MCP scheme in a spatially and temporally discrete fashion.

To this end, we will introduce an MCP model to define the probability of a state switch (Section 3.1), lay out how a state switch affects the local elastic and internal variables (Section 3.2), and integrate the time evolution of the thus-obtained recrystallization model with the RVE-level mechanical boundary value problem (Section 3.3). The overall incremental realization of the stochastic model is illustrated in Fig. 2.

3.1. Monte-Carlo-Potts model: probability of state switching

In order to capture the stochastic nature of state switches, we adopt an MCP-like approach (Potts, 1952; Anderson et al., 1984; Srolovitz et al., 1984a,b; Rollett et al., 1992; Janssens et al., 2010). Unlike the model of Ising (1925) which restricts the total number of states to two, our MCP model accounts for as many degenerate states as there are grains present at any given time (and the number of grains, n_G, is allowed to change in case of the nucleation of new grains or the consumption of existing grains). Instead of checking all n points inside the RVE for a potential state switch, we randomly select $n_{\text{MC,GBM}}, n_{\text{MC,NCL}} \ll n$ representative points for GBM/NCL at each time step and check which of

[4] We use Greek indices for time steps to avoid confusion with classical index notation.

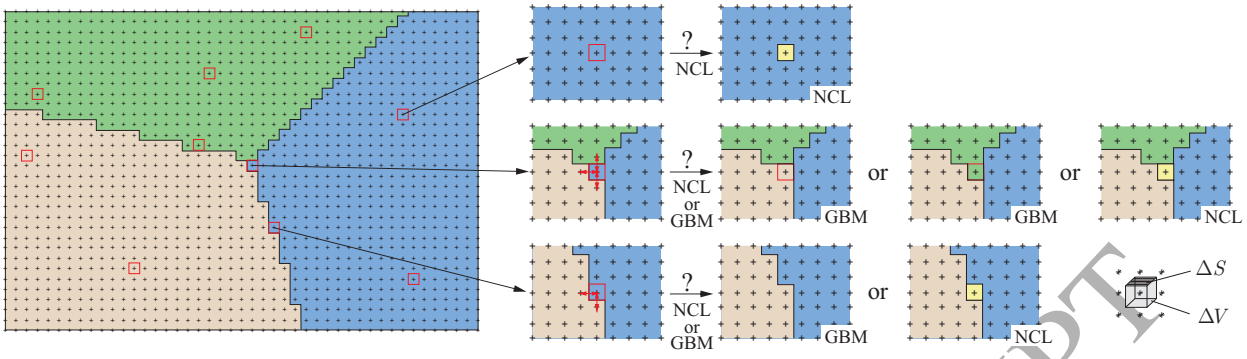

Figure 2: Schematic view of the state switch procedure: $n_{\mathrm{MC,GBM}}$ MCP sampling points are chosen from only those grid points adjacent to GBs, and $n_{\mathrm{MC,NCL}}$ sampling points from all n grid points. For each chosen grid point, possible options for state switches include the nucleation of a new grain (shown in yellow) or the adaption of the grain orientation of one of the neighboring points across a GB. In the latter case, the current energy $\mathcal{I}$ of each chosen sampling point is compared to its energy $\tilde{\mathcal{I}}$ after a possible state switch, by adopting the orientation of a neighboring grid point lying within an adjacent grain; the probability of switching depends on the energy difference $E = \tilde{\mathcal{I}} - \mathcal{I}$. Shown is also the definition of volume element ΔV and surface element ΔS.

those will undergo a state switch based on the criteria to be defined in Section 3.2. In a variation of the classical MCP model, we choose the $n_{\mathrm{MC,GBM}}$ points exclusively from those grid points adjacent to the GBs inside the RVE, whereas the $n_{\mathrm{MC,NCL}}$ points are generally chosen from the n grid points. For proper scaling, we choose $n_{\mathrm{MC,GBM}} \propto n^{2/3}$ to conserve the number of MCP points chosen from the GBs. The specific choice of the ratios $m_{\mathrm{MC},i} = n/n_{\mathrm{MC},i}$ (with i = GBM or NCL) naturally introduces the characteristic time scales of recrystallization. As shown in Section 4, the speed of migrating GBs is preserved if the discrete time step is chosen according to $\Delta t \propto n^{-1/3} = N^{-1}$. We further adopt the scaling for $n_{\mathrm{MC,NCL}} \propto \Delta t$ to control the nucleation rate.

The driving force behind a state switch is the reduction of stored energy. The total energy $\mathcal{I}$ of the RVE is composed of mechanical (Helmholtz) energy stored within Ω (including elastic and inelastic contributions) and interface energy concentrated in the GBs with surface energy density γ (and the collection of all GBs denoted by Γ), so that[5]

$$\begin{aligned}\mathcal{I} &= \int_\Omega A\left(\boldsymbol{F}(\boldsymbol{X}), \boldsymbol{F}^{\mathrm{in}}(\boldsymbol{X}), \boldsymbol{\varepsilon}(\boldsymbol{X}), \boldsymbol{\lambda}(\boldsymbol{X}); s(\boldsymbol{X})\right) \mathrm{d}V + \int_\Gamma \gamma(s_+, s_-)\mathrm{d}S \\ &\approx \Delta V \sum_{k=1}^{n} A\left(\boldsymbol{F}_k, \boldsymbol{F}_k^{\mathrm{in}}, \boldsymbol{\varepsilon}_k, \boldsymbol{\lambda}_k; s_k\right) + \Delta S \sum_{l=1}^{n_\Gamma} \gamma(s_{l^+}, s_{l^-}).\end{aligned} \tag{18}$$

Here, we approximate the total energy by a discrete sum over all n grid points in the RVE (each associated with a pixel volume ΔV), while the surface integral becomes a discrete sum over all n_Γ straight interface segments (each associated with a pixel surface ΔS); see Fig. 2. Note that the Helmholtz free energy is local and the dependence on state s is implicit through the slip and twin system orientations. The interface energy, in principle, depends on the two states s_{l^+} and s_{l^-} on both sides of a GB. For simplicity, we here assume a constant GB energy density γ_{S} which does not depend on misorientation, e.g., à la Read and Shockley (1950) or Wolf (1989). We note that misorientation-dependent GB mobilities (Winning et al., 2001; Winning and Rollett, 2005) or more complex boundary energy formulations (Ivasishin et al., 2006) can be readily included in our model but are neglected here.

Consider a local state switch from s_k to $\tilde{s}_k$, i.e., grid point k change its grain association, which comes with a change in crystal orientation as well as a change of $(\boldsymbol{F}_k, \boldsymbol{F}_k^{\mathrm{in}}, \boldsymbol{\varepsilon}_k, \boldsymbol{\lambda}_k)$ into some $(\tilde{\boldsymbol{F}}_k, \tilde{\boldsymbol{F}}_k^{\mathrm{in}}, \tilde{\boldsymbol{\varepsilon}}_k, \tilde{\boldsymbol{\lambda}}_k)$. Owing to the form of the energy in (18), the total change in energy due to this switch is local and given by

$$\Delta E = \tilde{\mathcal{I}} - \mathcal{I} = \Delta V\left[A\left(\tilde{\boldsymbol{F}}_k, \tilde{\boldsymbol{F}}_k^{\mathrm{in}}, \tilde{\boldsymbol{\varepsilon}}_k, \tilde{\boldsymbol{\lambda}}_k; \tilde{s}_k\right) - A\left(\boldsymbol{F}_k, \boldsymbol{F}_k^{\mathrm{in}}, \boldsymbol{\varepsilon}_k, \boldsymbol{\lambda}_k; s_k\right)\right] + \Delta S \sum_{l \in I_k} \gamma(s_k, s_l), \tag{19}$$

[5]For conciseness, here and in the following we implicitly include the position dependence at position $\boldsymbol{X}^k$ via subscripts $(\cdot)_k$, such that, e.g., $\boldsymbol{F}_k \equiv \boldsymbol{F}(\boldsymbol{X}^k)$, etc.

where I_k denotes the set of the six nearest-neighboring grid points of point k and

$$\gamma(s_k, s_j) = \gamma_S\, \delta(s_k, s_j) \qquad \text{with} \qquad \delta(s_k, s_j) = \begin{cases} 1 & \text{if } s_k = s_j, \\ 0 & \text{else,} \end{cases} \tag{20}$$

so that only interfaces between neighboring grid points associated with different grains contribute GB energy.

Based on the above energy difference and in analogy to the well-established Glauber dynamics (Glauber, 1963), acceptance thresholds are defined as

$$w_{\mathrm{GBM}}(\Delta E) = \frac{1}{2}\left[1 - \tanh\left(\frac{\Delta E - \Delta E_{\mathrm{cr,GBM}}}{k_B T_s}\right)\right], \qquad w_{\mathrm{NCL}}(\Delta E) = \frac{1}{2}\left[1 - \tanh\left(\frac{\Delta E - \Delta E_{\mathrm{cr,NCL}}}{k_B T_s}\right)\right] \tag{21}$$

with Boltzmann's constant k_B, an effective temperature T_s, and a constant $\Delta E_{\mathrm{cr}} > 0$.

Threshold (21) is used to decide, given a potential energy release ΔE_k, whether or not a material point k switches state by either NCL or GBM. If any of the $n_{\mathrm{MC}} = n_{\mathrm{MC,GBM}} + n_{\mathrm{MC,NCL}}$ sampling points is identified to have $\Delta E_k < 0$ for a possible state switch, a random number $\xi \sim \mathcal{U}[0, 1]$ is generated following a uniform distribution $\mathcal{U}[0, 1]$. The new state is accepted if $\xi \leq w(\Delta E_k)$ and rejected if $\xi > w(\Delta E_k)$. Since increasing ΔE_{cr} decreases the threshold $w(\Delta E)$ for a given ΔE (see Fig. 3), $\Delta E_{\mathrm{cr,GBM}}$ aims at capturing the dissipative drag of GBM while $\Delta E_{\mathrm{cr,NCL}}$ sets a nucleation threshold. All MCP model parameters used in subsequent simulations are summarized in Table 1.

Table 1: MCP model parameters chosen for the subsequent simulations of dynamic recrystallization, unless otherwise noted.

T_S [K]	γ_S [Jm^{-2}]	$\Delta E_{\mathrm{cr,NCL}}$ [MJm^{-3}]	$\Delta E_{\mathrm{cr,GBM}}$ [MJm^{-3}]
386	0.38	−1.00	−0.60

3.2. *Monte-Carlo-Potts model: state switches*

The calculation of ΔE_k requires comparing the currently stored energy $A(\boldsymbol{F}_k, \boldsymbol{F}_k^{\mathrm{in}}, \boldsymbol{\varepsilon}_k, \boldsymbol{\lambda}_k; s_k)$ to that of a hypothetical state $A(\tilde{\boldsymbol{F}}_k, \tilde{\boldsymbol{F}}_k^{\mathrm{in}}, \tilde{\boldsymbol{\varepsilon}}_k, \tilde{\boldsymbol{\lambda}}_k; \tilde{s}_k)$ after a state switch from s_k to $\tilde{s}_k$. Our definition of the latter state draws on recrystallization theory and experimental observations of grain nucleation and migration, and it is based on the following assumptions: (*i*) while nucleation is widely accepted to be predominantly driven by the reduction of elastic strain energy (Totten et al., 2004; Sreekala and Haataja, 2007), migration is caused by various driving forces associated with the minimization of the total stored energy (Totten et al., 2004), comprising interfacial as well as (in-)elastic bulk energy. (*ii*) Nucleation is observed to result in pristine, dislocation-starved grains (Al-Samman and Gottstein, 2008; Hallberg, 2011; Huang and Logé, 2016), as imposed in the phase field model of Chen et al. (2015). (*iii*) While the literature generally speaks of GBM as an advective process, little is known about the remains of existing dislocations interacting with migrating GBs (Sakai et al., 2014). Here, we presume that any material point which joins an adjacent grain will adopt that grain's crystallographic orientation and slip and twin systems in the *current configuration*, implying that

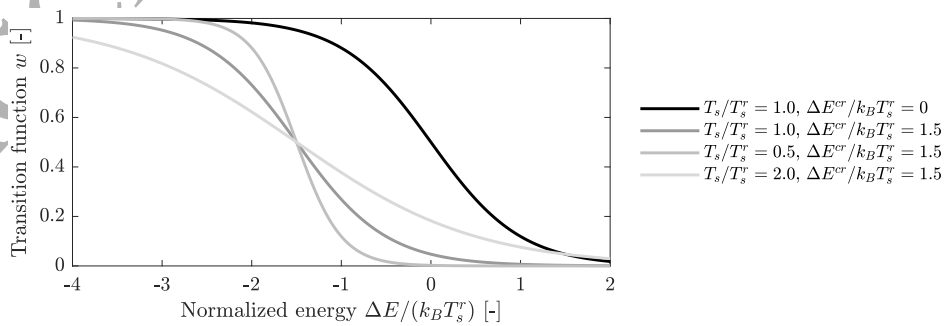

Figure 3: Acceptance threshold w as a function of the (normalized) energy difference for various values of T_S and ΔE_{cr} (normalized by some reference temperature T_s^r).

not only the state $\tilde{s}$ is adopted but also the elastic and inelastic deformation gradients, since, e.g., the slip system in the current configuration is given by $\left(\boldsymbol{F}^{\mathrm{e}}\boldsymbol{s}, (\boldsymbol{F}^{\mathrm{in}})^{\mathrm{T}}\boldsymbol{m}\right)$. Overall, this motivates defining the state switch such that

$$\tilde{\boldsymbol{F}}_k^{\mathrm{in}} = \begin{cases} \boldsymbol{I} \\ \boldsymbol{I} \end{cases} \qquad \tilde{\boldsymbol{F}}_k^{\mathrm{e}} = \begin{cases} \boldsymbol{I} \\ \boldsymbol{F}^{\mathrm{e,neighbor}} \end{cases} \qquad \tilde{\boldsymbol{\varepsilon}}_k = \begin{cases} \boldsymbol{0} \\ \boldsymbol{\varepsilon}^{\mathrm{neighbor}} \end{cases} \qquad \tilde{\boldsymbol{\lambda}}_k = \begin{cases} \boldsymbol{0} & \text{(NCL)} \\ \boldsymbol{\lambda}^{\mathrm{neighbor}} & \text{(GBM)} \end{cases} \tag{22}$$

where the superscript $(\cdot)^{\mathrm{neighbor}}$ refers to a neighboring material point already associated with grain $\tilde{s}_k$. We note that this choice is the authors' conclusion informed by both physical as well as numerical considerations in lack of sufficiently insightful experimental data. Appendix B discusses alternative approaches that were investigated. Since this method differs from previous MCP models (where at most one internal variable was subject to state switches), we refer to this model as a *Field Monte Carlo Potts* (FMCP) model.

Importantly, we also aim to maintain the same total deformation for compatibility, i.e., $\tilde{\boldsymbol{F}}_k = \boldsymbol{F}_k$, which unfortunately renders the constraints (22) mutually exclusive since $\tilde{\boldsymbol{F}}_k = \tilde{\boldsymbol{F}}_k^{\mathrm{e}}\tilde{\boldsymbol{F}}_k^{\mathrm{in}} = \boldsymbol{F}^{\mathrm{e,neighbor}} \neq \boldsymbol{F}_k$ in general. Therefore, we modify the deformation gradient decomposition by introducing a relative configuration $\boldsymbol{F}^{\mathrm{r}}$ such that

$$\boldsymbol{F} = \boldsymbol{F}^{\mathrm{e}}\boldsymbol{F}^{\mathrm{r}}\boldsymbol{F}^{\mathrm{in}}. \tag{23}$$

The idea of a relative or residual deformation gradient was already introduced, e.g., by Simo (1988) as the tangent map of a superposed spatial diffeomorphism to some deformation mapping or by Asaro (1983), who used it to measure the reorientation of the lattice with respect to some tensile axis. When using the decomposition (23), (22) can be realized by setting $\boldsymbol{F}^{\mathrm{r}} = \boldsymbol{I}$ in the undeformed configuration at all material points and choosing

$$\tilde{\boldsymbol{F}}_k^{\mathrm{r}} = (\tilde{\boldsymbol{F}}_k^{\mathrm{e}})^{-1}\,\tilde{\boldsymbol{F}}_k\,(\tilde{\boldsymbol{F}}_k^{\mathrm{in}})^{-1} \tag{24}$$

upon each state switch to satisfy compatibility. This also admits a physical interpretation since upon GBM the material point now adopts the slip and twin system orientations of the adjacent grain (in the current configuration).

(22) along with (23), (24) and $\tilde{\boldsymbol{F}}_k = \boldsymbol{F}_k$, completely defines a local state switch at a MCP sampling point k and admits calculating the potential energy differences ΔE_k (for every possible state switch considering the nearest-neighboring grid points of k). Fig. 4 illustrates the update process upon state switching, explained in the following.

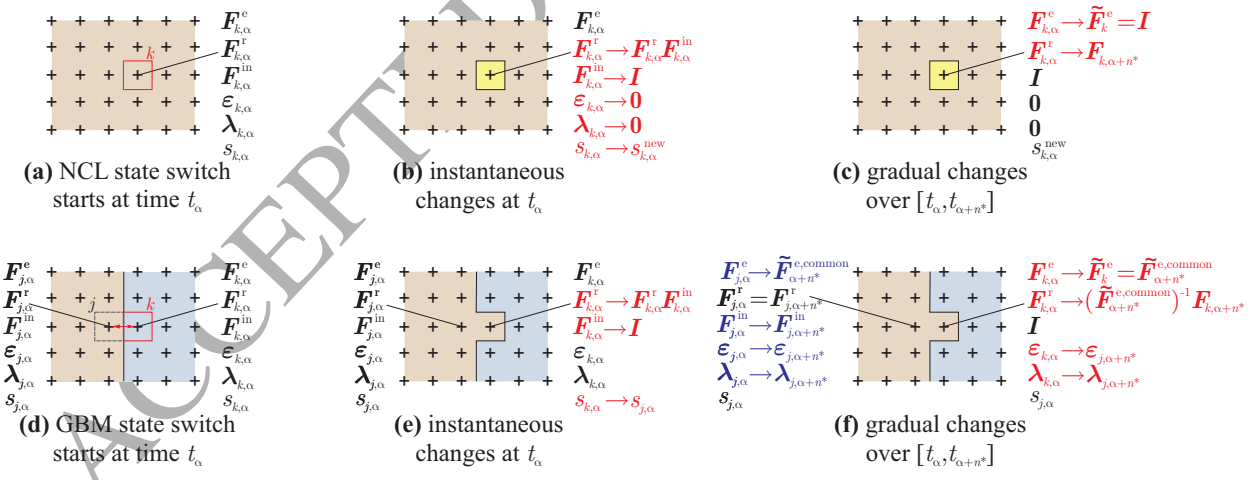

Figure 4: Visualization of the update process for NCL (**a-c**) and GBM (**d-f**): (**a,d**) selection of a sampling point k (*marked in red*) and – in the case of GBM – its neighboring reference point j (*marked in black*) at time t_α, (**b,e**) instantaneous update of the inelastic variables at time t_α, and (**c,f**) gradual update of $\boldsymbol{F}_k^{\mathrm{r}}$ over time $[t_\alpha, t_{\alpha+n^*}]$ along with mechanical equilibration at each time step, resulting in the matching of $\boldsymbol{F}_k^{\mathrm{e}}$ of the chosen sampling point k with identity in the case of NCL and that of the neighboring grid point j in the adjacent grain at the end of the process in the case of GBM. Imposed changes are *red*, while changes resulting from mechanical equilibration appear in *blue*.

3.3. *Monte-Carlo-Potts model: Incremental realization of a state switch*

An instantaneous switch of $\boldsymbol{F}^{\mathrm{e}}_k \to \tilde{\boldsymbol{F}}^{\mathrm{e}}_k$ would result in considerable convergence problems in the RVE-level boundary value problem (caused by sudden changes in the elastic/inelastic fields and the associated resolved shear stresses), which is why the following gradual update protocol is chosen. In a nutshell, the instantaneous state switch is spread over a finite time window Δt^* – which is in line with dynamic recrystallization being a continuous physical process[6].

We assume that the inelastic variables $(\boldsymbol{F}^{\mathrm{in}}_k, \boldsymbol{\varepsilon}_k, \boldsymbol{\lambda}_k; s_k)$ – which are tied to the atomic-level crystallographic configuration – change spontaneously and instantaneously into $(\tilde{\boldsymbol{F}}^{\mathrm{in}}_k, \tilde{\boldsymbol{\varepsilon}}_k, \tilde{\boldsymbol{\lambda}}_k; \tilde{s}_k)$. By contrast, the transition from $\boldsymbol{F}^{\mathrm{e}}_k$ to $\tilde{\boldsymbol{F}}^{\mathrm{e}}_k$ is performed gradually, since it is tied to the long-range elastic fields involving both the material point and relaxation mechanisms in its vicinity. It is important to note that we cannot control $\boldsymbol{F}^{\mathrm{e}}_k$ directly (only through $\boldsymbol{F}_k$, $\boldsymbol{F}^{\mathrm{in}}_k$ and $\boldsymbol{F}^{\mathrm{r}}_k$). Since $\boldsymbol{F}^{\mathrm{in}}_k \to \tilde{\boldsymbol{F}}^{\mathrm{in}}_k$ instantaneously as described above, we control $\boldsymbol{F}^{\mathrm{r}}_k$ to adjust $\boldsymbol{F}^{\mathrm{e}}_k \to \tilde{\boldsymbol{F}}^{\mathrm{e}}_k$. Moreover, we gradually change $\boldsymbol{F}^{\mathrm{e}}_k$ into $\tilde{\boldsymbol{F}}^{\mathrm{e}}_k$ over a time period Δt^* through an incremental sequence of $n^* = \lceil \Delta t^*/\Delta t \rceil$ mechanical equilibria (where Δt denotes the time step size of the simulation); see the schematic in Fig. 5. As the final state of this gradual update (starting at same time t_α and continuing over n^* times steps), we must have $\boldsymbol{F}^{\mathrm{e}}_{k,\alpha+n^*} = \tilde{\boldsymbol{F}}^{\mathrm{e}}_k$ from (22) – i.e., either $\boldsymbol{F}^{\mathrm{e}}_{k,\alpha+n^*} = \boldsymbol{I}$ for NCL, or $\boldsymbol{F}^{\mathrm{e}}_{k,\alpha+n^*} = \boldsymbol{F}^{\mathrm{e}}_{j,\alpha+n^*} = \tilde{\boldsymbol{F}}^{\mathrm{e,common}}_{\alpha+n^*}$ (which is a-priori unknown at t_α) for GBM, see Fig. 4. In summary, this implies that the selected MCP sampling point instantaneously adopts its new crystallography, then experiences an elastic-plastic evolution over Δt^* to continuously adjust grid point k to its target elastic state, thus achieving a relaxation of the stress state by continuous equilibration in the neighborhood of point k.

In order to gradually change $\boldsymbol{F}^{\mathrm{e}}$ in a physically sensible manner, we use the polar decomposition theorem to write $\boldsymbol{F}^{\mathrm{e}} = \boldsymbol{R}^{\mathrm{e}}\boldsymbol{U}^{\mathrm{e}}$ with rotation $\boldsymbol{R}^{\mathrm{e}} = \boldsymbol{F}^{\mathrm{e}}(\boldsymbol{U}^{\mathrm{e}})^{-1} \in \mathrm{SO}(3)$ and principal stretch tensor $\boldsymbol{U}^{\mathrm{e}} = \sqrt{(\boldsymbol{F}^{\mathrm{e}})^{\mathrm{T}}\boldsymbol{F}^{\mathrm{e}}} \in \mathrm{GL}(3)$. The gradual transformation from some given initial elastic deformation gradient $\boldsymbol{F}^{\mathrm{e}}_{k,\alpha}$ to the target elastic deformation gradient $\tilde{\boldsymbol{F}}^{\mathrm{e,target}}_{\alpha+n^*}$ is therefore accommodated by an iterative adjustment of, individually, stretch and rotation[7].

If at time t_α grid point k (with reference neighbor j in the case of GBM) has been identified for a state switch, we carry out the gradual update over time steps $\beta \in [\alpha, \alpha + n^*]$ so that $\boldsymbol{F}^{\mathrm{e}}_{k,\alpha} \to \tilde{\boldsymbol{F}}^{\mathrm{e}}_k$ from (22). We introduce tensors $\hat{\boldsymbol{R}}_\beta$ and $\hat{\boldsymbol{U}}_\beta$ as follows to define the stretch and rotational contributions to the elastic deformation mapping required to take point k towards its target at any time step β:

$$\boldsymbol{F}^{\mathrm{e}}_{k,\beta}\,\hat{\boldsymbol{F}}_\beta = \begin{cases} \boldsymbol{I} & \text{(NCL)} \\ \boldsymbol{F}^{\mathrm{e}}_{j,\beta} & \text{(GBM)} \end{cases} \qquad \text{with some} \quad \hat{\boldsymbol{F}}_\beta = \hat{\boldsymbol{R}}_\beta\,\hat{\boldsymbol{U}}_\beta, \quad \hat{\boldsymbol{R}}_\beta \in \mathrm{SO}(3),\ \hat{\boldsymbol{U}}_\beta \in \mathrm{GL}(3). \tag{25}$$

We break n^* down into $(n^* - n_U)$ and n_U time steps for adjusting the stretches and rotations, respectively. Following the arguments outlined above, the update of the elastic deformation at point k at time step $\beta + 1$ is thus defined recursively

[6] Recrystallization experiments are usually conducted on time scales significantly larger than the characteristic microscale relaxation times, which makes it difficult to extract information on the exact time-dependent evolution mechanisms. Nonetheless, we here propose a continuous update procedure for the microstructural states as a stable numerical scheme that simultaneously serves as a reasonable hypothesis of the actual kinetic microstructural evolution.

[7] Note that by definition, since $\det \boldsymbol{F}^{\mathrm{in}} = 1$ as well as $\det \boldsymbol{F} > 0$ and $\det \boldsymbol{F}^{\mathrm{r}} > 0$ by construction, $\boldsymbol{F}^{\mathrm{e}}$ is always invertible.

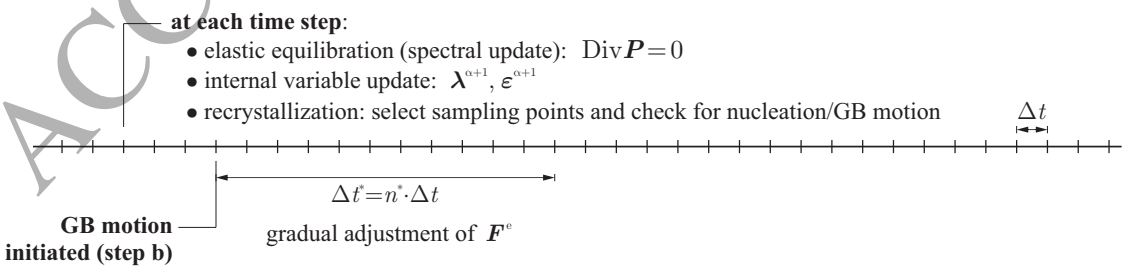

Figure 5: Schematic illustration of the time stepping scheme: at each time step the RVE is equilibrated, internal variables are updated, and n_{MC} sampling points are checked for grain nucleation or migration. If either is initiated (step b from Fig. 4), then the scheme of Fig. 4 starts, including a gradual adjustment of $\boldsymbol{F}^{\mathrm{e}}$ through adjusting $\boldsymbol{F}^{\mathrm{r}}$ over n^* time steps.

as

$$\boldsymbol{F}^{\mathrm{e}}_{k,\beta+1} = \begin{cases} \boldsymbol{F}^{\mathrm{e}}_{k,\beta}\hat{\boldsymbol{U}}_{\beta}^{-\frac{1}{n_U-(\beta-\alpha)}} & \text{for} \quad \beta \in \{\alpha,\dots,\alpha+n_U-1\} \\ \boldsymbol{F}^{\mathrm{e}}_{k,\beta}\hat{\boldsymbol{U}}_{\beta}^{-1}\hat{\boldsymbol{R}}_{\beta}^{-\frac{1}{n^*-(\beta-\alpha)}} & \text{for} \quad \beta \in \{\alpha+n_U,\dots,\alpha+n^*-1\}, \end{cases} \tag{26}$$

This scheme ensures that $\boldsymbol{F}^{\mathrm{e}}_{k,\alpha+n^*}$ equals its target value, viz. $\boldsymbol{F}^{\mathrm{e}}_{k,\alpha+n^*} = \boldsymbol{I}$ for NCL and $\boldsymbol{F}^{\mathrm{e}}_{k,\alpha+n^*} = \boldsymbol{F}^{\mathrm{e}}_{j,\alpha+n^*} = \tilde{\boldsymbol{F}}^{\mathrm{e,common}}_{\alpha+n^*} \in$ GL(3) for GBM. We note that, while (26) is being applied, mechanical equilibration including updates of the internal variables is also enforced, so that all fields are continuously evolving. The choice of the exponents in (26) is such that, in the hypothetical case of the absence of any changes to $\boldsymbol{F}^{\mathrm{e}}$ by mechanical equilibration, the incremental stretches and rotations applied during each step are constant. (The physics-informed scheme (26) is not restricted to recrystallization but can be applied in any constitutive framework where instantaneous state switches are to be avoided.) An algorithmic summary of the statistical model described in this section is provided in Table 1.

Recall that, although the elastic deformation gradient is adjusted gradually according to (26), the update of the inelastic deformation gradient occurs instantaneously at time step α. The same applies to the local orientation $s_k \to s_j$ (which is unproblematic for elastic isotropy but may require special treatment for anisotropic elastic energy densities).

4. Verification of the numerical scheme: Scaling and Convergence

We first verify that our model is appropriate to yield results independent of grid size as to demonstrate convergence with grid refinement, before proceeding to polycrystalline benchmark simulations. This is particularly important due to the statistical FMCP model for recrystallization: while the crystal plasticity setup is size-independent and therefore expected to converge with h-refinement, the FMCP model is based on randomly selecting $n_{\mathrm{MC,GBM}}$ and $n_{\mathrm{MC,NCL}}$ grid points for GBM and NCL, respectively. Those parameters – together with the time step Δt – affect results when changing the grid resolution, so that their values must be rescaled appropriately. To this end, Section 3.1 proposed a scaling aimed at proper convergence of results, which is verified here.

In our simulations the grid spacing is set to $\Delta X = 2.55\ \mu$m. Stochastic models such as the MCP model are generally not endowed with a physical length scale, so fitting with experiments is required to relate their numerical length scale to a physical one. Leaving the size of the RVE unchanged would result in $\Delta X \propto n^{-1/3}$, which in turn would influence the recrystallization kinetics due to changes in the balance between bulk energy and interface energy (scaling as $\Delta V \propto (\Delta X)^3$ and $\Delta S \propto (\Delta X)^2$, respectively). Therefore, when investigating different RVE resolutions in the following, we automatically imply a respective scaling of the RVE size to circumvent the aforementioned issues. Motivated by the deformation during ECAE, in subsequent benchmark tests we apply the average deformation gradient $\boldsymbol{F}^*(t) = \boldsymbol{I} + \dot{\gamma}_{\mathrm{sh}} t\, \boldsymbol{e}_1 \otimes \boldsymbol{e}_3$ with $\dot{\gamma}_{\mathrm{sh}}$ denoting the applied shear rate.

4.1. Scaling of the number of MCP sampling points with changing grid size for GBM

A proper rescaling of $n_{\mathrm{MC,GBM}}$, the number of MCP sampling points for GBM, with the total number of grid points, n, is essential to ensure convergence of the effective GBM kinetics (e.g., GBM speeds) with RVE refinement. To test the chosen scheme, a bicrystal having c-axis misorientations of $\pm\pi/16$ with respect to the [101] pole and a misorientation of $\pi/8$ to one another is subjected to the controlled nucleation of a new grain at the RVE center, whose c-axis is aligned with the [101] pole (see Fig. 6). Suppressing any other nucleation, we test if the chosen scaling leads to comparable results of the GBM kinetics by comparing $n_{\mathrm{MC,GBM}} = 8$, 18 and 32 on grids with, respectively, $n = 32^3$, 48^3 and 64^3 points (along with properly rescaled Δt) according to the scaling relations of Section 3.1. For accelerated albeit stable results in this example, we here use $T_S = 300$K, $\gamma_S = 0.31\mathrm{Jm}^{-2}$ and $\Delta E_{\mathrm{cr,GBM}} = -0.05\mathrm{Jm}^{-3}$.

Fig. 6 illustrates how the qualitative migration behavior is conserved across the three grid resolutions, thanks to properly rescaled $n_{\mathrm{MC,GBM}}$ and Δt. While the growing volume and surface of the new grain compare well between resolutions (cf. Fig. 7), differences appear in terms of the non-smooth grain surface (despite identical GB energy γ_S). The shape of the GB becomes smoother and more regular with increasing n, especially at low strain levels. An increasingly similar migration behavior towards higher strains both in terms of propagation velocity as well as surface smoothness leads to the conclusion that the chosen scaling indeed leads to mesh-independent results in the limit of negligible surface penalization effects, which is approximately reached at higher strains, where the difference in Helmholtz free energy dominate the effects of surface penalization.

Algorithm 1 Incremental update algorithm applied at each time step α.

1. **Update the macroscopic/average deformation gradient** to $\boldsymbol{F}^{*}_{\alpha+1}$
2. **Application of the FFT-based method to solve the elastic RVE problem** (at fixed internal variables):
   - compute $\boldsymbol{F}_{k,\alpha+1} = \boldsymbol{F}(\boldsymbol{X}_k, t_{\alpha+1})\ \forall\, k \in \{1, ..., n\}$
3. **Update the internal variables** (at fixed deformation gradients):
   - compute $\boldsymbol{\epsilon}_{\alpha+1}(\boldsymbol{X}_k)$, $\boldsymbol{\lambda}_{\alpha+1}(\boldsymbol{X}_k)$, $\boldsymbol{F}^{\mathrm{in}}_{\alpha+1}(\boldsymbol{X}_k)\ \ \forall\, k \in \{1, \dots, n\}/(\mathcal{S}_{\mathrm{GBM}} \cup \mathcal{S}_{\mathrm{NCL}})$
   - compute $\boldsymbol{F}^{\mathrm{e}}_{\alpha+1}(\boldsymbol{X}_k) = \boldsymbol{F}_{\alpha+1}(\boldsymbol{X}_k)\left(\boldsymbol{F}^{\mathrm{r}}_{\alpha+1}(\boldsymbol{X}_k)\boldsymbol{F}^{\mathrm{in}}_{\alpha+1}(\boldsymbol{X}_k)\right)^{-1}\ \ \forall\, k \in \{1, \dots, n\}/(\mathcal{S}_{\mathrm{GBM}} \cup \mathcal{S}_{\mathrm{NCL}})$,

   where $\mathcal{S}_{\mathrm{GBM}}$ and $\mathcal{S}_{\mathrm{NCL}}$ denote the sets of nodes that currently undergo a state change in the sense of GBM and NCL, respectively (i.e., those points are within their n^{*} time steps to accommodate the state switch).
4. **Monte-Carlo-Potts acceptance/rejection**:
   - randomly select $n_{\mathrm{MC,GBM}}$ and $n_{\mathrm{MC,NCL}}$ grid points from the set of, respectively, all GB-adjacent and all grid points (not considering those in $\mathcal{S}_{\mathrm{GBM}} \cup \mathcal{S}_{\mathrm{NCL}}$)
   - for each of the $n_{\mathrm{MC,GBM}}$ grid points (by considering all nearest-neighboring points for reference):
     – compute the minimal $\Delta E_{\mathrm{GBM}} < 0$ and associated $w^{\mathrm{thresh}}_{\mathrm{GBM}} = w_{\mathrm{GBM}}(\Delta E_{\mathrm{GBM}})$
     – generate a random number ξ_{GBM}
     – if $\xi_{\mathrm{GBM}} \leq w^{\mathrm{thresh}}_{\mathrm{GBM}}$: insert grid point into $\mathcal{S}_{\mathrm{GBM}}$
   - for each of the $n_{\mathrm{MC,NCL}}$ grid points (by considering a random orientation for the new grain):
     – compute ΔE_{NCL} and $w^{\mathrm{thresh}}_{\mathrm{NCL}} = w_{\mathrm{NCL}}(\Delta E_{\mathrm{NCL}})$
     – generate a random number ξ_{NCL}
     – if $\xi_{\mathrm{NCL}} \leq w^{\mathrm{thresh}}_{\mathrm{NCL}}$: insert grid point into $\mathcal{S}_{\mathrm{NCL}}$
5. **Monte-Carlo-Potts updates**:
   for each $k \in \mathcal{S}_{\mathrm{GBM}} \cup \mathcal{S}_{\mathrm{NCL}}$:
   - if point k has just been inserted during this time step α:
     – if $k \in \mathcal{S}_{\mathrm{GBM}}$: set $\boldsymbol{s}_{0,i} \leftarrow \boldsymbol{s}_{0,j}$ and $\boldsymbol{m}_{0,i} \leftarrow \boldsymbol{m}_{0,j}$, where j denotes the neighboring reference node whose grain association is being advected
     – if $k \in \mathcal{S}_{\mathrm{NCL}}$: set $\boldsymbol{s}_{0,i} \leftarrow \boldsymbol{s}_{0,\mathrm{new}}$ and $\boldsymbol{m}_{0,i} \leftarrow \boldsymbol{m}_{0,\mathrm{new}}$ for a new *random* orientation of the nucleated grain
   - update $\boldsymbol{F}^{\mathrm{e}}_{k,\alpha} \rightarrow \boldsymbol{F}^{\mathrm{e}}_{k,\alpha+1}$ according to (26) by changing $\boldsymbol{F}^{\mathrm{r}}_{k,\alpha} \rightarrow \boldsymbol{F}^{\mathrm{r}}_{k,\alpha+1}$,
     if $k \in \mathcal{S}_{\mathrm{GBM}}$: set $\boldsymbol{\varepsilon}_{k,\alpha+1} \leftarrow \boldsymbol{\varepsilon}_{j,\alpha+1}$ and $\boldsymbol{\lambda}_{k,\alpha+1} \leftarrow \boldsymbol{\lambda}_{j,\alpha+1}$, where j denotes the neighboring reference node whose grain association is being advected
   - if α is the n^{*}-th increment for grid point k (completing the state switch):
     – if $k \in \mathcal{S}_{\mathrm{GBM}}$: remove k from $\mathcal{S}_{\mathrm{GBM}}$
     – if $k \in \mathcal{S}_{\mathrm{NCL}}$: remove k from $\mathcal{S}_{\mathrm{NCL}}$

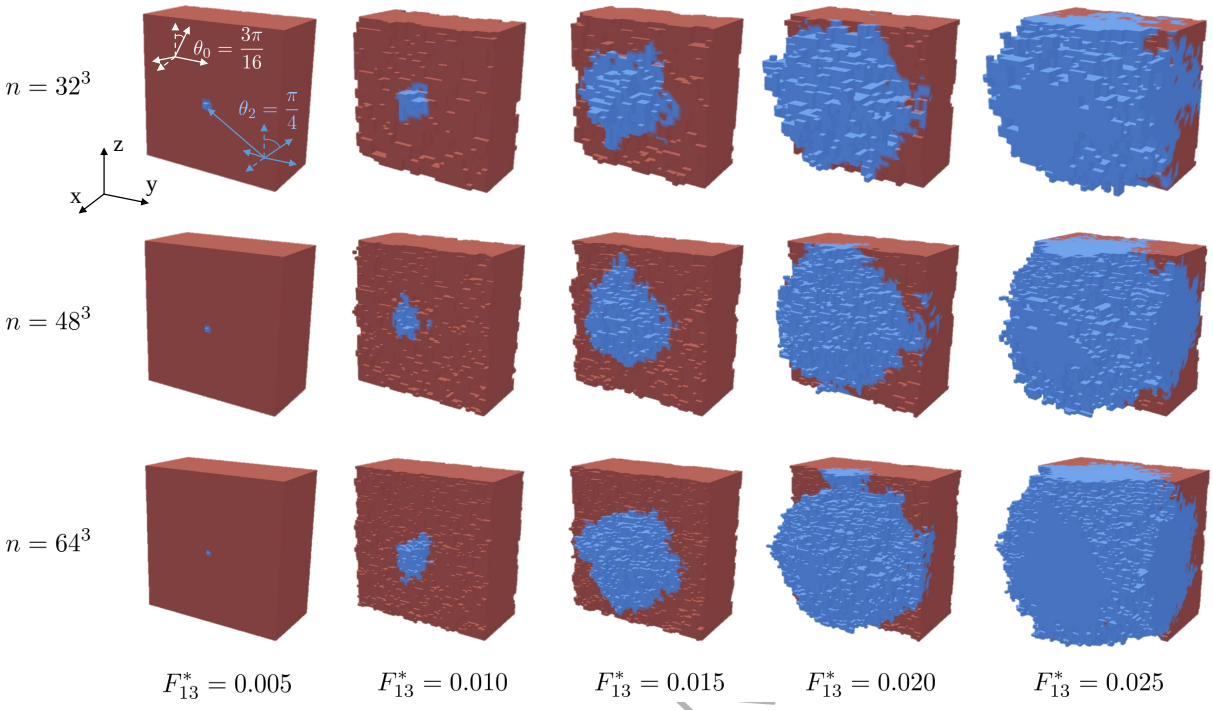

Figure 6: Comparison of GBM for a newly nucleated grain (shown in *blue*) embedded within a bicrystal (only one of the two original crystals is shown in *red*) for $n = 32^3$ (*top*), $n = 48^3$ (*center*) and $n = 64^3$ (*bottom*), when using the scaling relations introduced in Section 3.1. The five snapshots are taken at different average strain levels, using the aforementioned simple shear setup.

4.2. *Scaling of the number of MCP sampling points with changing grid size for NCL*

Having verified proper scaling of the effective kinetics for GBM, we next study the chosen MC scheme for NCL. As a benchmark, we investigate a polycrystal composed of initially 128 grains with randomly distributed c-axis misorientations within $\leq \pi/16$ from the [101] axis. The choice of a [101]-biased texture is due to relatively poor basal slip under the prescribed simple shear, which promotes prismatic and $\langle c + a \rangle$-slip and thus showcases the full capabilities of the model to treat severe inelastic anisotropy. Due to inconsequential observations about the correlation between initial grain orientations and NCL during recrystallization, we consider the pseudo-random initial texture around the [101]-pole appropriate[8].

We use the parameters of Table 1 and rescale $n_{\mathrm{MC,GBM}}$ and $n_{\mathrm{MC,NCL}}$ for three different grid sizes n, as discussed in Sections 3.1 and 4.1. Fig. 8 compares the effective RVE stress–strain response for different choices of n, showing convincing agreement. Deviations are observed at larger strains predominantly for the secondary recrystallization cycle. The reduction in peak stress for the relatively coarse choice of $n = 32^3$ is explained by the fact that, with increasing n, the $n_{\mathrm{MC,NCL}}$ points selected for potential NCL increasingly lie away from GB triple-junctions, which are energetically preferable sites for nucleation but statistically less often sampled with increasing n.

As a further illustration, the histograms in Fig. 9 show the changes in the relative grain sizes (measured as fractions of the RVE volume) for the three discretization levels of Fig. 8. As expected, recrystallization leads to a reduction in the average grain size as well as to a spread in the grain size distribution. A stronger shift towards smaller grain sizes with decreasing grid resolution emphasizes the aforementioned increased nucleation activity at lower resolutions due to the increased probability of selecting MCP points near triple-junctions. However, overall results – both the effective stress–strain response and the microstructural changes – tend to converge with increasing grid resolution.

[8] For example, Al-Samman and Gottstein (2008) showed that for specific combinations of process temperature and strain rate, texture randomization in Mg alloys could be observed; yet, the emergence of random textures (as opposed to highly textured microstructures) varied with initial microstructure and no clear trend can be concluded.

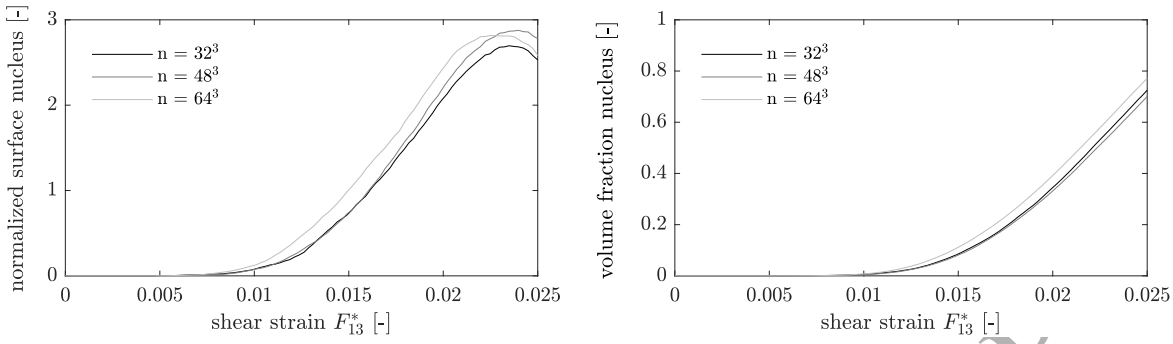

(a) Surface of the nucleus normalized by the RVE's surface area(b) Volume of the nucleus normalized by the RVE's total volume

Figure 7: Quantitative comparison of the volume and surface area of the newly nucleated grain in Fig. 6, demonstrating grid size-independent GBM kinetics across three different RVE discretizations with $n = 32^3, 48^3, 64^3$.

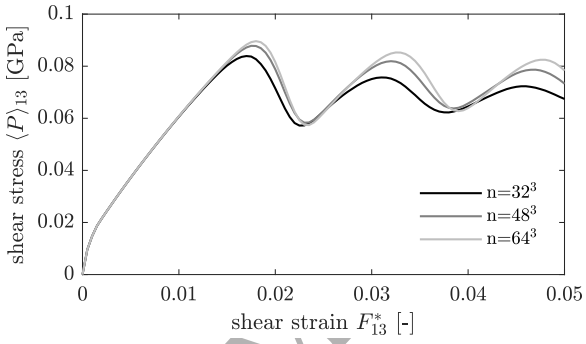

Figure 8: Comparison of the average shear stress $P^*_{13} = \langle P_{13} \rangle$ vs. average shear strain F^*_{13} for $n = 32^3, 48^3, 64^3$, using the scaling of the number of MCP sampling points with n as introduced in Section 3.1.

4.3. Dependence of the homogenized behavior on statistical MCP sampling

Although our FMCP approach is stochastic and therefore expected to yield different results when repeated even under identical initial conditions, comparable effective material behavior (i.e., evolution of both macroscopic stresses and microstructural statistics) is expected for sufficiently large RVEs and statistically similar initial orientation distributions (e.g., chosen from a fixed range of orientations around a given pole, as discussed above). As an ensemble study, we conducted four simulations with identical initial microstructures, differing merely by the random seed used for the MCP point selection. Fig. 10 illustrates the results of two different examples, each having 128 initial grains but with their initial textures spread around the [101]-pole by less than either $\pi/16$ or $\pi/8$. For both cases, the differences in the homogenized stress–strain response between the four runs is small with the highest relative deviations in the stresses found around 3.5% and 4.2% for the scenarios with, respectively, lower and higher misorientations. Based on the relatively low amount of basal slip for grains with a rotation close to $\pi/4$ under this shear loading, a higher inelastic strain energy density is attained through increased prismatic and particularly pyramidal slip. This accelerated rise of the inelastic energy density in return causes nucleation at relatively low average strains. The shift in nucleation initiation of the individual recrystallization cycles thus ultimately causes the observable difference in the number of cycles passed until the final strain of $F^*_{13} = 0.05$.

5. Results: Microstructural evolution and resulting stress–strain response during ECAE

Motivated by the prevalent simple shear deformation in the process zone of ECAE, the macroscopic load history for all subsequent examples has the form $\boldsymbol{F}^*(t) = \boldsymbol{I} + \dot{\gamma}_{\mathrm{sh}} t\, \boldsymbol{e}_1 \otimes \boldsymbol{e}_3$, where $\dot{\gamma}_{\mathrm{sh}}$ denotes the shear rate (which for quasistatics is set to $\dot{\gamma}_{\mathrm{sh}} = 10^{-5}\ \mathrm{s}^{-1}$). The low strain rate allows us to replicate the multi-peak stress–strain behavior

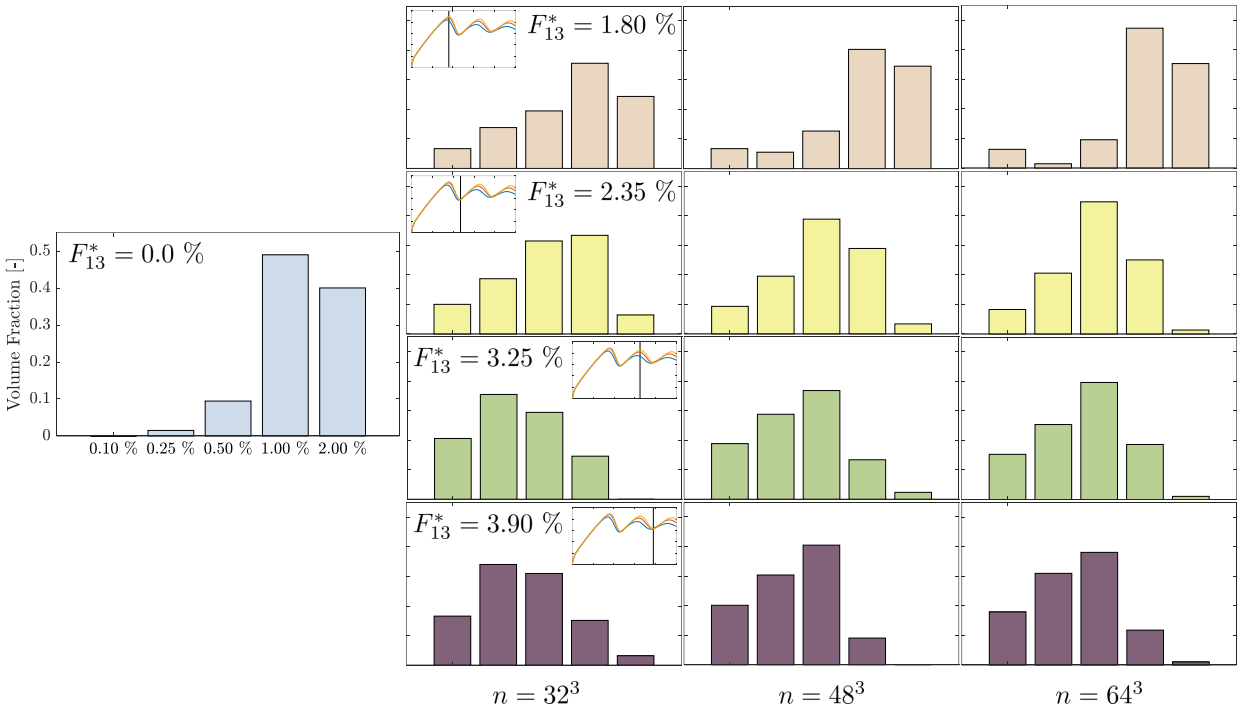

Figure 9: Evolution of the grain size distribution shown as histograms of RVE volume fractions of the grain volumes, thresholded by $\{0.10\%, 0.25\%, 0.50\%, 1.0\%, 2.0\%\}$ for average shear strain levels of 1.80% (*red*), 2.35% (*yellow*), 3.25% (*green*) and 3.90% (*purple*) as compared to the initial distribution (*blue*, on the left) for $n = 32^3$ (*left*), $n = 48^3$ (*center*) and $n = 64^3$ (*right*).

characteristic of low-strain-rate/high-temperature discontinuous dynamic recrystallization, in which periods of pure inelastic deformation and of recrystallization can be distinguished, which, in turn, allows us to more cleanly inspect the effects of the various model parameters. In conformity with a classic ECAE setup endowed with a 90° turn, the extrusion direction (ED), transverse direction (TD) and normal direction (ND) are in our setup, respectively, the positive x-axis, positive y-axis and negative z-axis. The incremental time step is set to $\Delta t = 0.5$ s for the case of $n = 64^3$ ($N = 64$) and accordingly scaled for all other discretizations. All investigations are conducted up to a maximum strain[9] of $\gamma_{\text{sh,max}} = \dot{\gamma}_{\text{sh}} t_{\text{max}} = 0.05$.

We investigate a polycrystal with initially 128 randomly oriented grains with a maximum misorientation of $\pi/8$ from the [101]-pole. Fig. 11 illustrates the evolution of the homogenized shear stress $P^*_{13} = \langle P_{13} \rangle$ with the applied shear strain F^*_{13}. Following an initial phase of recrystallization-free elastic-plastic deformation, the onset of nucleation is identified by the stress decrease due to the nucleation of new grains (near point B). The subsequent growth of those pristine grains by GBM alongside further NCL causes a continuing decrease of the homogenized stress up to point D, where the entire RVE is consumed by the nucleated grains. The fully recrystallized RVE then undergoes, again, elastic-plastic deformation resulting in a rising average stress. When the inelastic strain energy is again sufficiently high to increase the probability of nucleation, recrystallization results in another stress reduction – overall thus resulting in the classical *multi-peak* stress–strain behavior observed at low strain rates (Hallberg, 2011). For higher strain rates, the distinction between time periods in which recrystallization-free deformation is dominant vs. periods in which NCL

[9]We note that the simulation temperature for both GBM and NCL was set in such a way to observe recrystallization at strains below those observed in experiments (which is beneficial for computational efficiency at such low strain rates). The reason for this choice lies in the nature of the material parameters present in the Mg constitutive model, which were fitted to room-temperature data (Chang and Kochmann, 2015). This is significantly below the temperatures at which dynamic recrystallization investigations are conducted and thus only allows the underlying material model to function in a stable manner at low strains. The inclusion of temperature-dependent models is, however, readily possible, in which case recrystallization can be captured at the experimentally observed strain levels. The simulation temperature is thus exploited for rescaling, which enables large-strain effects at smaller strain levels.

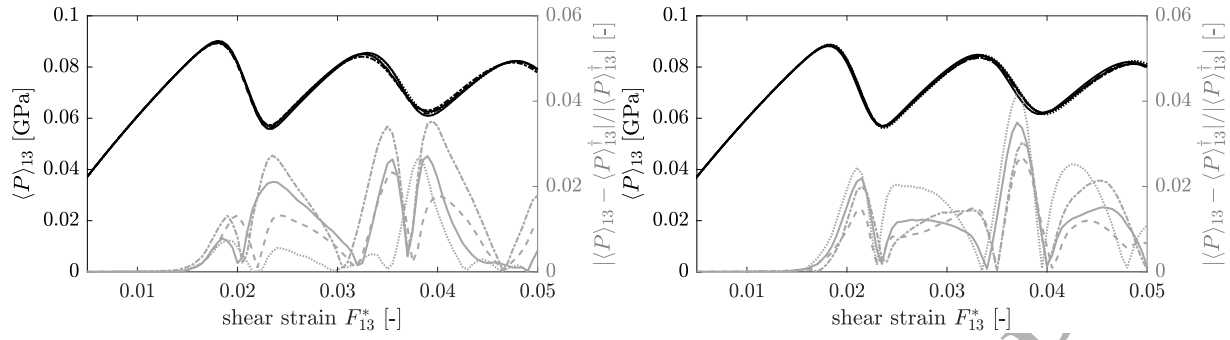

Figure 10: Illustration of the (negligible) influence of the random seed used for MCP sampling point selection under otherwise identical conditions including the same initial microstructure comprising 128 grains with two misorientation ranges of the c-axis with respect to the [101]-pole, viz. $\pi/16$ (*left*) and $\pi/8$ (*right*). Each set of four curves corresponds to four repeated runs (relative errors are computed with respect to a fifth run whose homogenized stress levels are referred to as $\langle P^{\dagger}_{13}\rangle$).

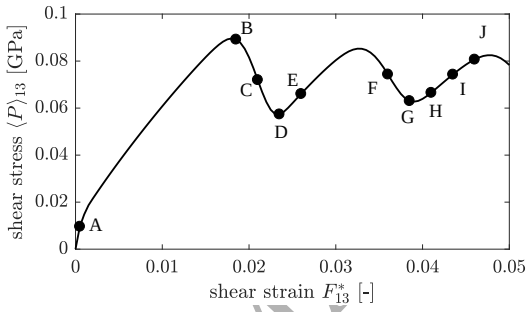

Figure 11: Evolution of the $P^{*}_{13} = \langle P_{13}\rangle$ shear stress vs. the applied shear strain F^{*}_{13}. Markers denote the strains corresponding to the grain, shear stress and inelastic strain energy density distributions across the RVE shown in Figs. 13, 12 and 14, respectively.

and GBM are prevalent vanishes gradually. This ultimately results in the classic *single-peak* stress–strain behavior (Hallberg, 2011; Rossard and Blain, 1959; Blaz et al., 1983), which can also be capture by the present model depending on model parameters and will be discussed in Section 6.

To elucidate the underlying mesoscale mechanisms, Figs. 13, 12 and 14 illustrate the distributions of, respectively, the grains, the $\langle P_{13}\rangle$ stress, and the inelastic strain energy density (as a driving force for discontinuous dynamic recrystallization) across the RVE. All three illustrations clearly support the identification of the individual stages in which NCL vs. GBM vs. elastic/inelastic deformation is dominant (labels in Figs. 13–14 correspond to the strain levels in Fig. 11). The two recrystallization waves become apparent in Fig. 13 which illustrates the newly nucleated grains. The onset of each wave corresponds to states of high stresses and of high stored energy as seen in Figs. 12 and 14. In addition, a decrease of the average grain size is observable throughout the two recrystallization cycles as mentioned in Section 4.2 (cf. the decrease in average grain size in Fig. 9).

It is interesting to compare the above results with a classical model for dynamic recrystallization frequently used in the literature. The JMAK relation (Kolmogorov, 1937; Johnson and Mehl, 1939; Avrami, 1939) approximates the evolution of the volume fraction of recrystallized material, $\eta_{\mathrm{RX}} \in [0, 1]$, in the form

$$\eta_{\mathrm{RX}}(t) = 1 - \exp\left(-\int_{t_{\mathrm{RX}}}^{t} v(\tau)\,\dot{n}_{\mathrm{NCL}}(\tau)\,\mathrm{d}\tau\right) \approx 1 - \exp(-A(t - t_{\mathrm{RX}})^{p}), \tag{27}$$

where $v(\tau)$ and $\dot{n}_{\mathrm{NCL}}(\tau)$ define, respectively, the reference volume and nucleation rate within previously unrecrystallized material at time τ. $A, p \in \mathbb{R}^{+}$ describe constants dependent on both the material as well as the processing route; p is commonly referred to as the Avrami coefficient. t_{RX} is defined as the time at which recrystallization starts, which we set to the time at which 1.0% of the RVE is recrystallized for a fair comparison with the JMAK model. In contrast to our high-fidelity model, JMAK assumes simple GB kinetics (e.g., a constant nucleation rate and a constant growth

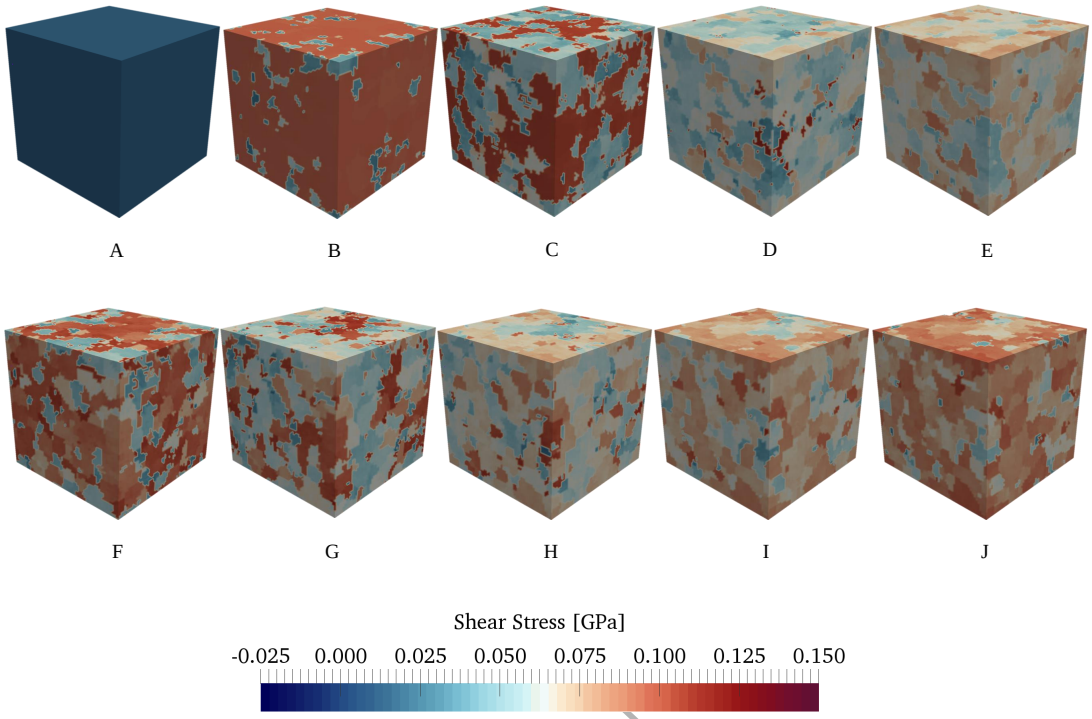

Figure 12: Evolution of the P_{13} shear stress distribution at the ten strain levels marked in Fig. 11. The initiation and completion of each recrystallization wave agrees well with the, respectively, highest and lowest stresses found across the RVE.

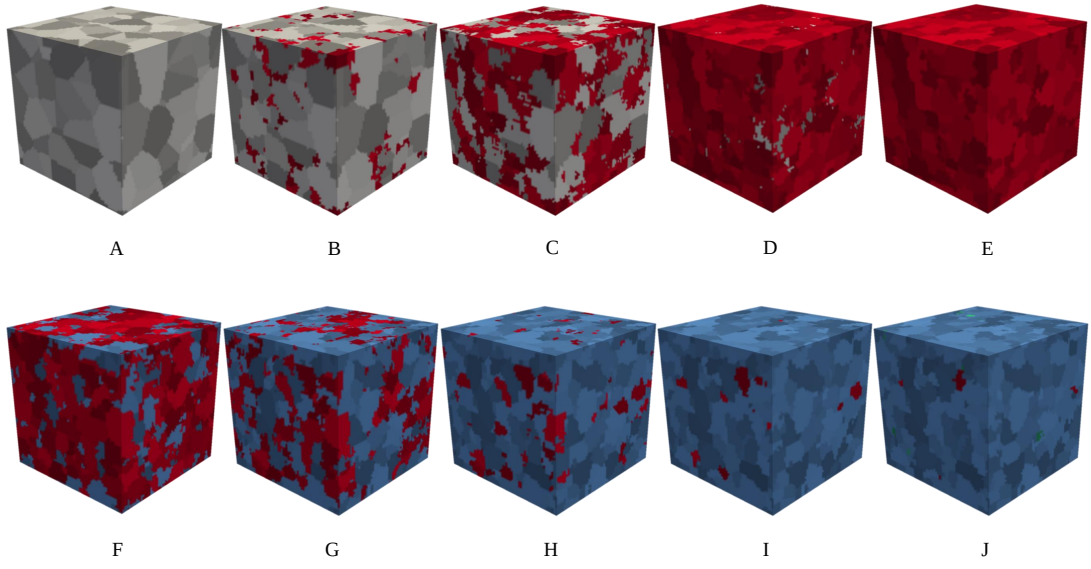

Figure 13: Evolution of the grain distribution, shown at the strain levels marked by points A through J in Fig. 11: the color code emphasizes the microstructural evolution from the initial grain structure (*gray*) through a first recrystallization wave (new grains shown in *red*) and a second recrystallization wave (new grains in *blue*). The observed recrystallization waves correlate well with the stress–strain behavior of Fig. 11.

velocity, thus neglecting any local effects (Raabe, 2002)). Since JMAK has been frequently used to infer recrystallization specifics (Raabe, 1999, 2002; Ivasishin et al., 2006; Bernacki et al., 2009), it is interesting to compare (27) to the results found here.

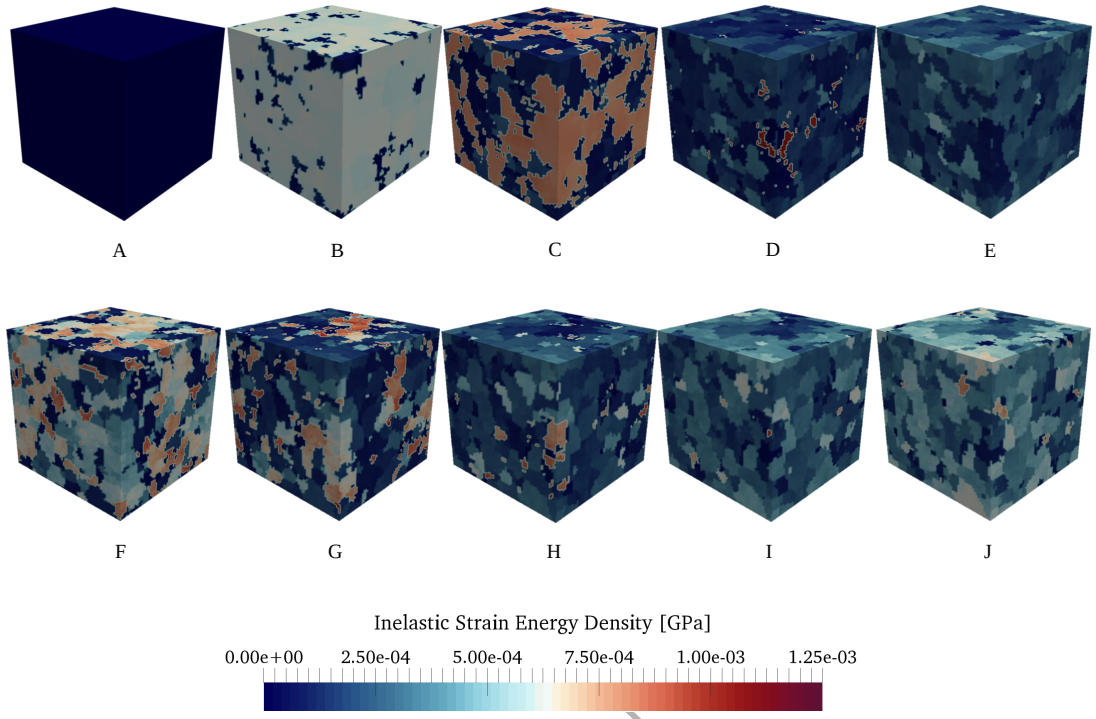

Figure 14: Evolution of the inelastic strain energy density $W^{\mathrm{sl}} + W^{\mathrm{tw}}$ at the ten strain levels marked in Fig. 11. Each recrystallization wave is associated with a decrease in the accumulated stored energy density through the nucleation and growth of grains.

Fig. 15 plots the evolution of η_{RX} as obtained from the simulations in Section 5. According to (27), we expect $\log\left[-\log\left(1-\eta_{\mathrm{RX}}\right)\right]$ to scale linearly with $(t - t_{\mathrm{RX}})$, and the slope is identified as the Avrami coefficient p. The shown scaling in Fig. 15 is more complex than linear, as can be expected from our high-fidelity model that circumvents the various assumptions underlying JMAK theory. When computing the slope of the obtained curve at $t - t_{\mathrm{RX}} = 100$s, 300s and 750s, we obtain coefficients $p = 0.64$, 3.0 and 5.3, respectively. Especially the obtained p-values at 300s and 750s (i.e., when recrystallization is well underway) agree well with the range of previously reported Avrami exponents of $p = 4.0$ (Doherty et al., 1993) and $p = 3.91$ (Bernacki et al., 2009), both for 3D simulations.

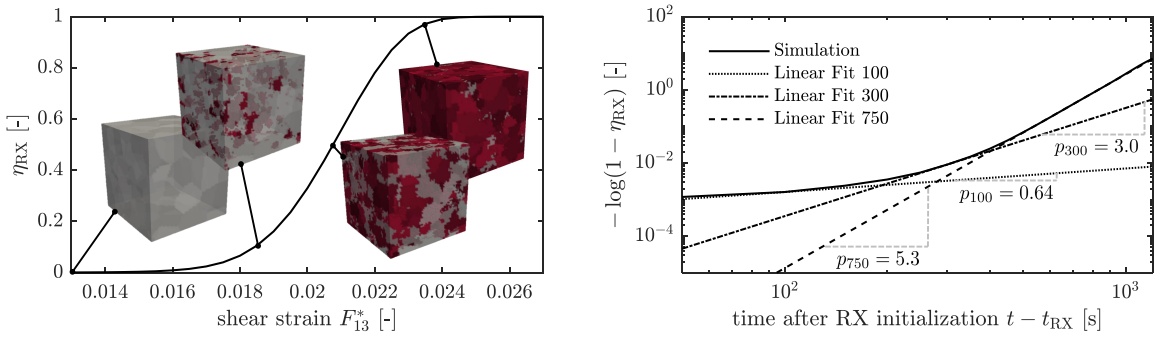

Figure 15: Evolution of volume fraction of recrystallized material as obtained from the simulations in Section 5, shown both on a linear (*left*) as well as on a double-logarithmic scale (*right*) with three representative slopes p computed at $t - t_{\mathrm{RX}} = 100$s, 300s, 750s.

6. Influence of the FMCP model parameters

The recrystallization kinetics in our model are governed by the probability of switching defined in (21). The latter depends on several model parameters whose influence is investigated in the following and shown to allow us to fine-tune the model for other applications involving variations in temperature and strain rate.

6.1. *Numerical temperature T_S*

Due to the lack of a suitable temperature-dependent material model for Mg, temperature T_S introduced in the probabilistic recrystallization kinetics does not imply a true process temperature. However, it is expected to qualitatively show the correct influence of temperature on the recrystallization kinetics through the thermally-activated migration and nucleation kinetics governed by (21). Fig. 16 illustrates the influence of changing T_S on the multi-peak stress–strain behavior and indeed reveals a reduction in peak stress and recrystallization wave period with increasing T_S. Since the underlying crystal plasticity model was calibrated for room temperature and invariant to changes in temperature, the shown results underestimate the reduction in peak stress with increasing temperature.

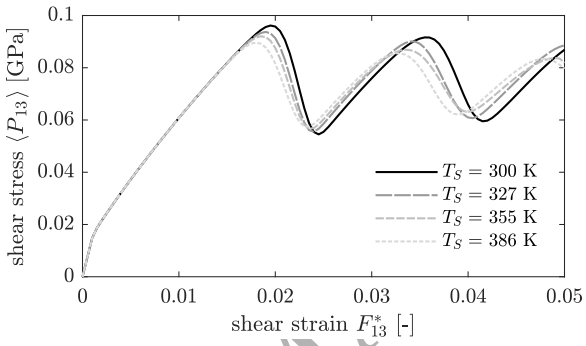

Figure 16: Influence of variations in the simulation temperature T_S on the multi-peak stress–strain behavior.

6.2. *Critical nucleation and migration thresholds $\Delta E_{cr,NCL}$ and $\Delta E_{cr,GBM}$*

Changes in the critical energy thresholds in (21) affect the recrystallization kinetics and enable the transition from a multi-peak to a single-peak stress–strain behavior, as shown in Fig. 17. In general, the transition from a serrated to a single-peak flow stress behavior is observed for increasing strain rates or decreasing temperatures (Rossard and Blain, 1959; Blaz et al., 1983; Hallberg, 2011), caused by the gradual overlapping of individual recrystallization waves due to accelerated inelastic deformation in the nucleated grains relative to a decreased migration behavior.

For fixed $n_{\mathrm{MC,GBM}}$, $n_{\mathrm{MC,NCL}}$ and T_S we may interpret changes in ΔE_{NCL} and ΔE_{GBM} by recourse to an empirical rule for the critical dislocation density for NCL (Roberts and Ahlblom, 1978; Hallberg, 2011),

$$\rho_{\mathrm{cr}} \sim \left(\frac{\gamma_S \dot{\epsilon}^{\mathrm{p}}_{\mathrm{eff}}}{blm\tau^2} \right)^{1/3}, \tag{28}$$

where b is the magnitude of the Burgers vector, l the dislocation mean-free path, m the GB mobility, $\tau = \mu b^2/2$ the dislocation line energy, and $\dot{\epsilon}^{\mathrm{p}}_{\mathrm{eff}}$ the phenomenological notion of a macroscopic plastic strain rate. In addition, empirical laws predict a variation of the nucleation rate $\dot{n}_{\mathrm{NCL}}$ with process parameters such as temperature and strain rate according to the classical form (Peczak and Luton, 1993; Hallberg, 2011)

$$\dot{n}_{\mathrm{NCL}} \sim \dot{\epsilon}^{\mathrm{p}}_{\mathrm{eff}} \exp\left(\frac{Q}{RT} \right), \tag{29}$$

where Q represents an activation energy, and R is the gas constant. Comparing (28) and (29) yields $\dot{n}_{\mathrm{NCL}}/\rho_{\mathrm{cr}} \sim \left(\dot{\epsilon}^{\mathrm{p}}_{\mathrm{eff}}\right)^{2/3}$. A relative decrease in ρ_{cr} with respect to the nucleation rate $\dot{n}_{\mathrm{NCL}} \sim n_{\mathrm{MC,NCL}}/\Delta t$ is therefore associated with an increase in $\dot{\epsilon}^{\mathrm{p}}_{\mathrm{eff}}$. Given $\Delta E_{\mathrm{cr,NCL}} \sim \rho_{\mathrm{cr}}$ (Mellbin et al., 2016), the tendency towards a single-peak flow stress evolution with decreasing $\Delta E_{\mathrm{cr,NCL}}$, as observed in Fig. 17, therefore agrees well with increasing strain rates.

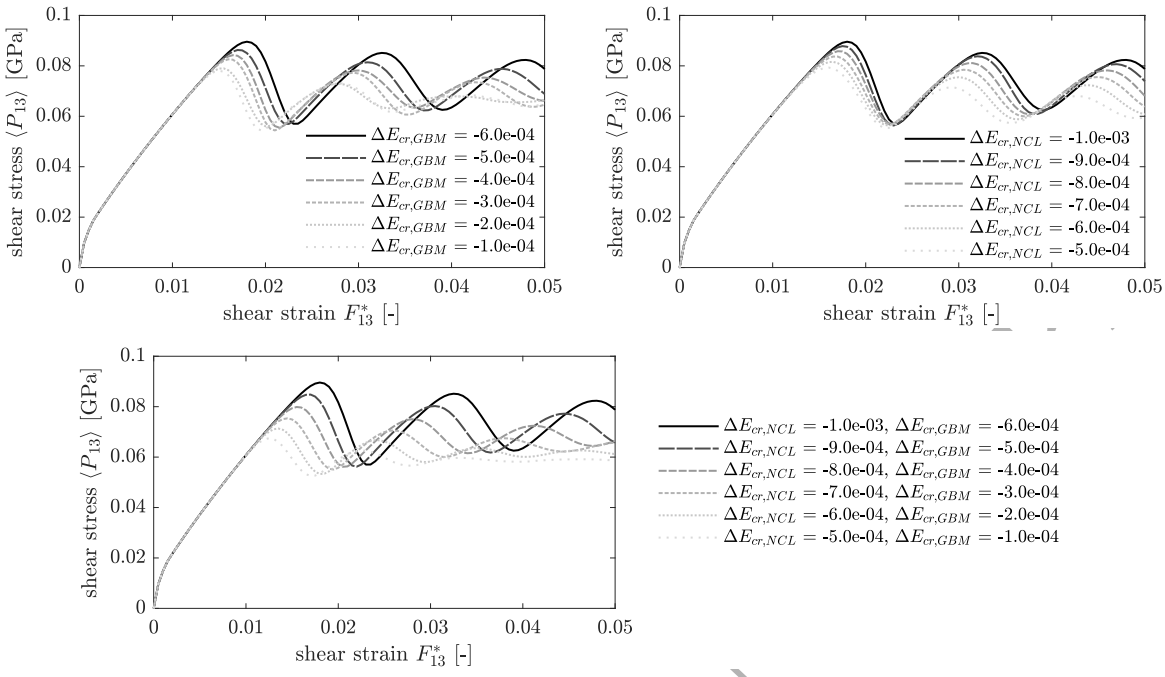

Figure 17: Effects of variations in $\Delta E_{\text{cr,NCL}}$ and $\Delta E_{\text{cr,GBM}}$ on the homogenized stress–strain behavior (all energy densities given in units of GPa). Unless otherwise indicated, the critical energy thresholds listed in Table 1 were used.

6.3. *Number of MCP sampling points*

The phenomenological relation for $\dot{n}_{NCL}$ in (29) captures the transition from multi- to single-peak stress–strain behavior with increasing strain rate and decreasing temperature. It was previously employed in phase field models (Takaki et al., 2008), cellular automata (Ding and Guo, 2001) as well as MCP models (Ivasishin et al., 2006), where the dependence on strain rate was, in principle, included in a term measuring the Hamiltonian change through nucleation. Practically, however, that Hamiltonian change was set to a constant, thus eliminating the dependence on strain rate.

In our approach, the Arrhenius-type dependence on temperature is captured through the modified Glauber dynamics, the dependence on strain rate emerges naturally from the rate-dependent constitutive model, and $\dot{n}_{NCL}$ is directly related to the choice of the number of MCP sampling points, $n_{\text{MC,NCL}}$. We examine the latter relationship by increasing $n_{\text{MC,NCL}}$, which, as shown in Fig. 18, decreases the peak stresses. This is explained through an increase in nucleation activity, not only by shifting the NCL probability to lower strain levels but also by increasing the total number of nuclei. At the same time, it does not significantly affect the multi-peak character of the stress–strain curve. By contrast, increasing $n_{\text{MC,GBM}}$ yields the expected more pronounced multi-peak stress–strain behavior, since an increased migration speed promotes the completion of individual recrystallization waves, thus making an overlap of recrystallization waves – as required for single-peak behavior – less likely.

7. Discussion

The previous sections demonstrated that the FMCP model introduced here provides a high-fidelity, mesh-independent technique for modeling discontinuous dynamic recrystallization at finite strains by NCL and GBM in a statistical fashion, whose kinetics are controlled by the FMCP model parameters – capturing both single- and multi-peak stress–strain behavior as well as qualitatively describing the influence of process temperature. While previous approaches – some of which were mentioned in Section 1 – showed advances in replicating the characteristic single- and/or multi-peak flow stress response for this type of recrystallization seen in experiments (see, e.g., Fig. 19), to the best of our knowledge, no previous model has presented a comparably general framework for arbitrary load paths and general, finite-strain constitutive models including deformation twinning.

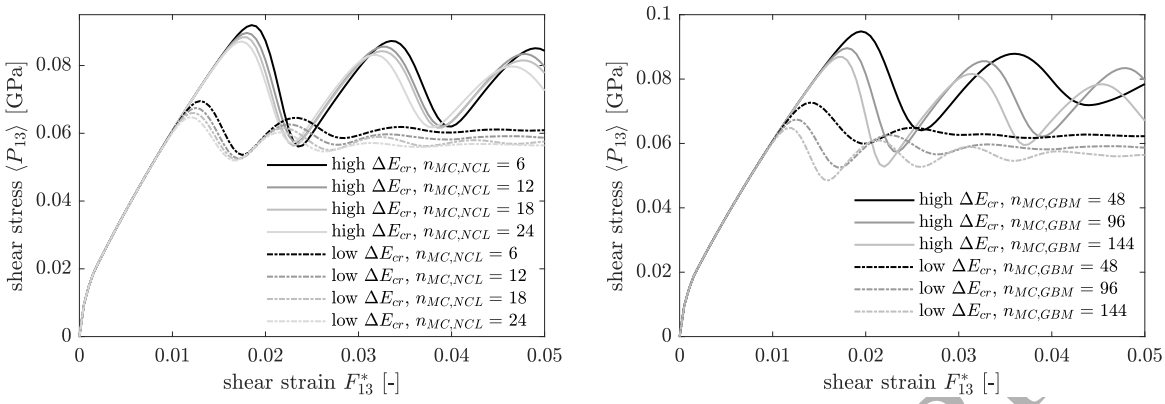

Figure 18: Effects of variations in $n_{\mathrm{MC,NCL}}$ and $n_{\mathrm{MC,GBM}}$ on the homogenized stress–strain behavior for *high* critical energy thresholds $\Delta E_{\mathrm{cr,NCL}} = -10^{-3}$ Jm^{-3} and $\Delta E_{\mathrm{cr,GBM}} = -6 \cdot 10^{-4}$ Jm^{-3}, and *low* $\Delta E_{\mathrm{cr,NCL}} = -5 \cdot 10^{-4}$ Jm^{-3} and $\Delta E_{\mathrm{cr,GBM}} = -10^{-4}$ Jm^{-3}.

In Section 6, we showed how the single- vs. multi-peak stress–strain behavior depends on the FMCP model parameters. A refined model (particularly including a temperature-aware crystal plasticity model) may hence be used to study the influence of process parameters such as temperature, loading rate and path.

Early recrystallization models were based on single scalar fields capturing the microstructure (such as the dislocation density; see, e.g., Takaki et al. (2008)), where the temporal evolution was frequently governed by the phenomenological model of Mecking and Kocks (1981) or an ad-hoc generated, oftentimes time-invariant stored energy field (see, e.g., Ivasishin et al. (2006)). Recent work combined cellular automata with crystal plasticity models to show how anisotropic inelasticity can be integrated into the framework of recrystallization (Popova et al., 2015). However, the way in which nucleation was implemented in those models could not describe the emergence of a second recrystallization wave and therefore restricted the simulations to a single recrystallization cycle.

The model presented here went from a pure description of GBM to an FMCP formulation that couples GBM and NCL, further using physically motivated state change definitions that take into account the full elastic and inelastic state of a material point. This not only allows us to capture multiple recrystallization waves but also leads to the convergence towards a steady state for rising strains as well as a transition between single- and multi-peak stress–strain behavior dependent on model parameters. Liao et al. (2014) observed exactly this transition, dependent on process temperature, for Mg alloy AZ61 (see Fig 19). The flexibility to capture this phenomenon in the model is readily given; yet, required is a careful parameter fitting as well as a temperature-aware constitutive model. Parameter identification is challenging when studying ECAE since stress–strain data are hard to extract from experimental force-displacements curves corrupted by friction in the device; therefore, alternative experimental setups may be preferable.

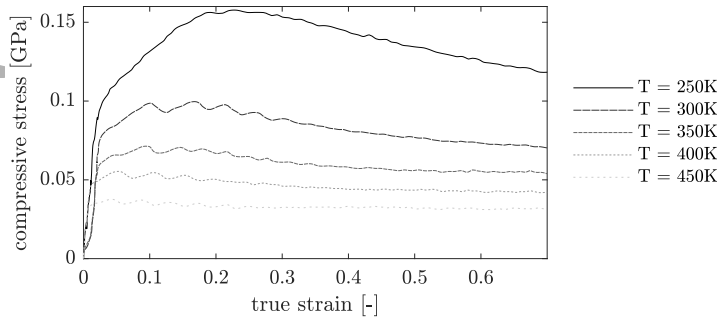

Figure 19: Evolution of the temperature-dependent single-to-multi-peak transition for Mg alloy AZ61 (Mg-6.1Al-1.1Zn-0.18Mn (wt%)) subjected to hot isothermal compression tests at a constant strain rate of $0.1 s^{-1}$ performed by a thermal simulation machine posterior to annealing conducted at 400°C for 60 min; data taken from (Liao et al., 2014).

We point out that the particular combination of the FMCP model with the grid-based FFT solver of the mechanical homogenization problem requires a careful treatment of local state switches, which was achieved by the gradual update procedure of Section 3.3. Abrupt local changes would cause numerical instability due to enormous jumps in the resolved shear stress on the individual slip and twin systems upon state switching. Our time-continuous interpretation of state switches – accommodated by individually adopting the new stretch and rotation – provides a physics-informed stabilization of the underlying mechanical solver. The presented formulation is sufficiently general to be applied to, in principle, arbitrary constitutive models that involve sudden changes of the fields of deformation, providing increased numerical stability while mechanical compatibility and invertability of the deformation gradient.

8. Conclusions

We presented a computational framework to model discontinuous dynamic recrystallization at finite strains while accounting for strongly anisotropic inelasticity as well as alternative strain-accommodating microstructural mechanisms such as deformation twinning in hcp metals. We combined an extended crystal plasticity model for Mg with a Monte-Carlo-Potts approach to recrystallization. The latter treats both grain nucleation and grain boundary migration in a statistical fashion, so that the kinetics of discontinuous dynamic recrystallization are described in a natural fashion that is based on the local energetics of the polycrystalline microstructure. The mechanical homogenization problem is solved on the RVE-level by recourse to an FFT-based solver whose regular spatial grids provides the natural basis for the described coupling to the discrete, stochastic Monte-Carlo framework. In addition, the FFT efficiency admits simulations at high spatial resolution. Simulation results showed that (*i*) the chosen Monte-Carlo protocol achieves convergence of the recrystallization kinetics with grid resolution, (*ii*) results are (to a good approximation) insensitive to the random selection of MCP sampling points, (*iii*) single- and multi-peak stress–strain behavior can be described by a single model, depending on model parameters that are linked to the microstructural mechanisms of recrystallization, (*iv*) the qualitative influence of process temperature is included, (*v*) the typical reduction in average grain size and an increasing spread in grain sizes is observed for ECAE simulations, *(vi)* the obtained effective recrystallization kinetics agree well with JMAK theory at sufficiently high strain levels (when recrystallization is well underway). The presented model is sufficiently general to apply to other constitutive models and can be coupled to temperature-aware constitutive models (without the scope of this investigation).

Acknowledgement

This research was sponsored by the Army Research Laboratory and was accomplished under Cooperative Agreement Number W911NF-12-2-0022. The views and conclusions contained in this document are those of the authors and should not be interpreted as representing the official policies, either expressed or implied, of the Army Research Laboratory or the U.S. Government. The U.S. Government is authorized to reproduce and distribute reprints for Government purposes notwithstanding any copyright notation herein.

Appendix A. Parameters used in the Mg material model

Table A.2 summarizes the material parameters based on the study of Chang and Kochmann (2015) to fully define the slip-twinning interaction model introduced in Section 2.1. Solely τ_0 differs from the parameter values used in Chang and Kochmann (2015), which was changed due to the switch from an implicit to an explicit model (see Chang et al. (2017)).

Table A.2: Material parameters used in the extended crystal plasticity model for Mg after Chang and Kochmann (2015). We note that parameter τ_0, the critical resolved shear stress, has been modified from the original model, since the formulation of Chang and Kochmann (2015) was used in an implicit context, whereas here we use an explicit formulation that does not suffer from numerical complications by introducing a hard threshold into the rate-dependent model; see also Chang et al. (2017).

elastic Lamé moduli

λ	μ
24.0	19.4
GPa	GPa

extension twins

h_0	k_{ij}	$\dot{\lambda}_0$	m_{tw}	γ_{tw}
1.7	40	1	1	0.129
MPa	GPa	-	-	-

basal slip (hardening & dissipation)

h_α	σ_∞	h_{ij}	τ_0	m	$\dot{\gamma}_0$
7.1	0.70	0	17.5	0.05	1.0
GPa	MPa	MPa	MPa	-	s^{-1}

prismatic slip (hardening & dissipation)

h_α	σ_∞	h_{ij}	τ_0	m	$\dot{\gamma}_0$
9.0	85	20	17.5	0.05	1.0
GPa	MPa	MPa	MPa	-	s^{-1}

pyramidal $\langle c+a \rangle$ slip (hardening & dissipation)

h_α	σ_∞	h_{ij}	τ_0	m	$\dot{\gamma}_0$
30	150	25	17.5	0.05	1.0
GPa	MPa	MPa	MPa	-	s^{-1}

Appendix B. Alternative definitions of state switches due to GBM

In Section 3.2 we presented a particular form of the local kinematic updates of the elastic state ($\boldsymbol{F}^{\text{e}}$) and the inelastic state ($\boldsymbol{F}^{\text{in}}$, $\boldsymbol{\varepsilon}$, $\boldsymbol{\lambda}$) associated with a state switch due to GBM, as defined by (22) and complemented by (24). We note that this choice is, of course, not unique. We therefore considered and discarded various alternatives which are briefly summarized here to justify the particular choices made:

- **Approach 1:** A moving GB can be interpreted as a reconfiguration front which leaves the region over which it has swept in a pristine, defect-free state. In terms of the state variables used in this model, this implies $\tilde{\boldsymbol{\varepsilon}}_k = \boldsymbol{0}$, $\tilde{\boldsymbol{\lambda}}_k = \boldsymbol{0}$, $\tilde{\boldsymbol{F}}^{\text{in}} = \boldsymbol{I}$ but $\tilde{\boldsymbol{F}}^{\text{e}} = \boldsymbol{F}^{\text{e}}$ and $\tilde{\boldsymbol{F}}^{\text{r}} = (\boldsymbol{F}^{\text{e}})^{-1}\boldsymbol{F}$, where the tilde denotes the state after the state switch. Unfortunately, a pristine elastic state would lead to excessively high local stresses which, in turn, translate into high flow stresses on certain slip systems. The latter is physically questionable and also leads to convergence failure of the crystal plasticity model employed here. Moreover, although the passage of a GB is expected to dissolve existing defect structures, the recovery of a completely pristine grain is physically unlikely.
- **Approach 2:** The above problem can be partially overcome by adding a complete relaxation of the stress state. In terms of the state variables this translates into $\tilde{\boldsymbol{\varepsilon}}_k = \boldsymbol{0}$, $\tilde{\boldsymbol{\lambda}}_k = \boldsymbol{0}$, $\tilde{\boldsymbol{F}}^{\text{in}} = \boldsymbol{I}$, $\tilde{\boldsymbol{F}}^{\text{e}} = \boldsymbol{I}$, and $\tilde{\boldsymbol{F}}^{\text{r}} = \boldsymbol{F}$. This, however, equates migration to nucleation, which has little physical justification and implies that severe local deformation gradients $\boldsymbol{F}$ may result in zero local stresses.
- **Approach 3:** In our approach, we assume that the inelastic state of a point that is passed by a migrating GB is independent of its history before GB arrival but affected by the plastic history and defect structure in the expanding grain. This translates into the update laws (22). Specifically by assuming that the elastic state of the neighboring grain is also adopted, we avoid the aforementioned excessive stress increase and – in conjunction with the time-continuous adoption process outlined in Section 3.3 – achieve numerical stability.

References

Agnew, S., Yoo, M., Tome, C., 2001. Application of texture simulation to understanding mechanical behavior of Mg and solid solution alloys containing Li or Y. Acta Materialia 49 (20), 4277–4289.

Al-Samman, T., Gottstein, G., 2008. Dynamic recrystallization during high temperature deformation of magnesium. Materials Science and Engineering: A 490 (1), 411–420.

Allen, S. M., Cahn, J. W., 1972. Ground state structures in ordered binary alloys with second neighbor interactions. Acta Metallurgica 20 (3), 423–433.

Anderson, M., Srolovitz, D., Grest, G., Sahni, P., 1984. Computer simulation of grain growth - I. Kinetics. Acta Metallurgica 32 (5), 783–791.

Asadi, P., Givi, M. K. B., Akbari, M., 2015. Microstructural simulation of friction stir welding using a cellular automaton method: a microstructure prediction of AZ91 magnesium alloy. International Journal of Mechanical and Materials Engineering 10 (1), 20.

Asaro, R. J., 1983. Micromechanics of crystals and polycrystals. In: Advances in Applied Mechanics. Vol. 23. Elsevier, pp. 1–115.

Avrami, M., 1939. Kinetics of phase change. i general theory. The Journal of Chemical Physics 7 (12), 1103–1112.

Bacca, M., Hayhurst, D. R., McMeeking, R. M., 2015. Continuous dynamic recrystallization during severe plastic deformation. Mechanics of Materials 90, 148–156.

Bernacki, M., Resk, H., Coupez, T., Logé, R. E., 2009. Finite element model of primary recrystallization in polycrystalline aggregates using a level set framework. Modelling and Simulation in Materials Science and Engineering 17 (6), 064006.

Blaz, L., Sakai, T., Jonas, J., 1983. Effect of initial grain size on dynamic recrystallization of copper. Metal Science 17 (12), 609–616.

Chang, Y., Kochmann, D. M., 2015. A variational constitutive model for slip-twinning interactions in hcp metals: application to single-and polycrystalline magnesium. International Journal of Plasticity 73, 39–61.

Chang, Y., Lloyd, J. T., Becker, R., Kochmann, D. M., 2017. Modeling microstructure evolution in magnesium: Comparison of detailed and reduced-order kinematic models. Mechanics of Materials 108, 40–57.

Chen, L., Chen, J., Lebensohn, R., Ji, Y., Heo, T., Bhattacharyya, S., Chang, K., Mathaudhu, S., Liu, Z., Chen, L.-Q., 2015. An integrated fast Fourier transform-based phase-field and crystal plasticity approach to model recrystallization of three dimensional polycrystals. Computer Methods in Applied Mechanics and Engineering 285, 829–848.

Christian, J. W., Mahajan, S., 1995. Deformation twinning. Progress in Materials Science 39 (1-2), 1–157.

Cram, D., Zurob, H., Brechet, Y., Hutchinson, C., 2009. Modelling discontinuous dynamic recrystallization using a physically based model for nucleation. Acta Materialia 57 (17), 5218–5228.

Ding, R., Guo, Z., 2001. Coupled quantitative simulation of microstructural evolution and plastic flow during dynamic recrystallization. Acta Materialia 49 (16), 3163–3175.

Doherty, R., Kashyap, K., Panchanadeeswaran, S., 1993. Direct observation of the development of recrystallization texture in commercial purity aluminum. Acta Metallurgica et Materialia 41 (10), 3029–3053.

Eisenlohr, P., Diehl, M., Lebensohn, R. A., Roters, F., 2013. A spectral method solution to crystal elasto-viscoplasticity at finite strains. International Journal of Plasticity 46, 37–53.

Estrin, Y., Mecking, H., 1984. A unified phenomenological description of work hardening and creep based on one-parameter models. Acta Metallurgica 32 (1), 57–70.

Fatemi-Varzaneh, S., Zarei-Hanzaki, A., Beladi, H., 2007. Dynamic recrystallization in AZ31 magnesium alloy. Materials Science and Engineering: A 456 (1-2), 52–57.

Fatemi-Varzaneh, S., Zarei-Hanzaki, A., Vaghar, R., 2013. Discontinuous dynamic recrystallization during accumulative back extrusion of a magnesium alloy. Journal of Ultrafine Grained and Nanostructured Materials 46 (1), 25–29.

Geers, M., Kouznetsova, V., Brekelmans, W., 2010. Multi-scale computational homogenization: Trends and challenges. Journal of Computational and Applied Mathematics 234 (7), 2175 – 2182.
URL http://www.sciencedirect.com/science/article/pii/S0377042709005536

Gentry, S., Thornton, K., 2015. Simulating recrystallization in titanium using the phase field method. In: IOP Conference Series: Materials Science and Engineering. Vol. 89. IOP Publishing, p. 012024.

Glauber, R. J., 1963. Time-dependent statistics of the ising model. Journal of Mathematical Physics 4 (2), 294–307.

Gourdet, S., Montheillet, F., 2003. A model of continuous dynamic recrystallization. Acta Materialia 51 (9), 2685–2699.

Graff, S., Brocks, W., Steglich, D., 2007. Yielding of magnesium: From single crystal to polycrystalline aggregates. International Journal of Plasticity 23 (12), 1957–1978.

Hall, E., 1951. The deformation and ageing of mild steel: III discussion of results. Proceedings of the Physical Society. Section B 64 (9), 747.

Hallberg, H., 2011. Approaches to modeling of recrystallization. Metals 1 (1), 16–48.

Hallberg, H., Wallin, M., Ristinmaa, M., 2010. Simulation of discontinuous dynamic recrystallization in pure Cu using a probabilistic cellular automaton. Computational Materials Science 49 (1), 25–34.

Homayonifar, M., Mosler, J., 2011. On the coupling of plastic slip and deformation-induced twinning in magnesium: A variationally consistent approach based on energy minimization. International Journal of Plasticity 27 (7), 983–1003.

Huang, K., Logé, R., 2016. A review of dynamic recrystallization phenomena in metallic materials. Materials & Design 111, 548–574.

Ising, E., 1925. Beitrag zur theorie des ferromagnetismus. Zeitschrift für Physik A Hadrons and Nuclei 31 (1), 253–258.

Ivasishin, O., Shevchenko, S., Vasiliev, N., Semiatin, S., 2006. A 3-D Monte-Carlo (Potts) model for recrystallization and grain growth in polycrystalline materials. Materials Science and Engineering: A 433 (1), 216–232.

Janssens, K. G. F., Raabe, D., Kozeschnik, E., Miodownik, M. A., Nestler, B., 2010. Computational materials engineering: An introduction to microstructure evolution. Academic Press.

Johnson, W. A., Mehl, R. F., 1939. Reaction kinetics in process of nucleation and growth. Transaction of AIME 135, 416–458.

Kabel, M., Böhlke, T., Schneider, M., 2014. Efficient fixed point and Newton–Krylov solvers for FFT-based homogenization of elasticity at large deformations. Computational Mechanics 54 (6), 1497–1514.

Kalidindi, S. R., 2001. Modeling anisotropic strain hardening and deformation textures in low stacking fault energy fcc metals. International Journal of Plasticity 17 (6), 837–860.

Kim, S. G., Kim, D. I., Kim, W. T., Park, Y. B., 2006. Computer simulations of two-dimensional and three-dimensional ideal grain growth. Physical Review E 74 (6), 061605.

Kolmogorov, A. N., 1937. On the statistical theory of the crystallization of metals. Bull. Acad. Sci. USSR, Math. Ser 1, 355–359.

Kouznetsova, V., Brekelmans, W. A. M., Baaijens, F. P. T., Jan 2001. An approach to micro-macro modeling of heterogeneous materials. Computational Mechanics 27 (1), 37–48.
URL https://doi.org/10.1007/s004660000212

Lebensohn, R. A., Kanjarla, A. K., Eisenlohr, P., 2012. An elasto-viscoplastic formulation based on fast Fourier transforms for the prediction of micromechanical fields in polycrystalline materials. International Journal of Plasticity 32, 59–69.

Lebensohn, R. A., Needleman, A., 2016. Numerical implementation of non-local polycrystal plasticity using fast Fourier transforms. Journal of the Mechanics and Physics of Solids 97, 333 – 351.
URL http://www.sciencedirect.com/science/article/pii/S0022509616301958

Liao, C., Wu, H., Wu, C., Zhu, F., Lee, S., 2014. Hot deformation behavior and flow stress modeling of annealed AZ61 mg alloys. Progress in Natural Science: Materials International 24 (3), 253–265.

Mecking, H., Kocks, U., 1981. Kinetics of flow and strain-hardening. Acta Metallurgica 29 (11), 1865–1875.

Mellbin, Y., Hallberg, H., Ristinmaa, M., 2016. Recrystallization and texture evolution during hot rolling of copper, studied by a multiscale model combining crystal plasticity and vertex models. Modelling and Simulation in Materials Science and Engineering 24 (7), 075004.

Metropolis, N., Rosenbluth, A. W., Rosenbluth, M. N., Teller, A. H., Teller, E., 1953. Equation of state calculations by fast computing machines. The Journal of Chemical Physics 21 (6), 1087–1092.

Miehe, C., Schröder, J., Becker, M., 2002. Computational homogenization analysis in finite elasticity: Material and structural instabilities on the micro- and macro-scales of periodic composites and their interaction. Computer Methods in Applied Mechanics and Engineering 191 (44), 4971–5005.
URL http://www.sciencedirect.com/science/article/pii/S0045782502003912

Moelans, N., Godfrey, A., Zhang, Y., Jensen, D. J., 2013. Phase-field simulation study of the migration of recrystallization boundaries. Physical Review B 88 (5), 054103.

Molkaraie, M., Gómez, V., 2015. Efficient monte carlo methods for the potts model at low temperature. arXiv preprint arXiv:1506.07044.

Moulinec, H., Suquet, P., 1994. A fast numerical method for computing the linear and nonlinear mechanical properties of composites. Comptes rendus de l'Académie des sciences. Série II, Mécanique, physique, chimie, astronomie 318 (11), 1417–1423.

Müller, W., 1998. Fourier Transforms and their application to the formation of textures and changes of morphology in solids. In: IUTAM Symposium on Transformation Problems in Composite and Active Materials. Kluwer Academic Publishers, pp. 61–72.

Ortiz, M., Repetto, E. A., 1999. Nonconvex energy minimization and dislocation structures in ductile single crystals. Journal of the Mechanics and Physics of Solids 47, 397–462.

Ortiz, M., Stainier, L., 1999. The variational formulation of viscoplastic constitutive updates. Computer Methods in Applied Mechanics and Engineering 171 (3-4), 419–444.

Peczak, P., Luton, M., 1993. The effect of nucleation models on dynamic recrystallization I. homogeneous stored energy distribution. Philosophical Magazine B 68 (1), 115–144.

Petch, N., 1953. The cleavage strengh of polycrystals. J. of the Iron and Steel Inst. 174, 25–28.

Popova, E., Staraselski, Y., Brahme, A., Mishra, R., Inal, K., 2015. Coupled crystal plasticity–probabilistic cellular automata approach to model dynamic recrystallization in magnesium alloys. International Journal of Plasticity 66, 85–102.

Potts, R. B., 1952. Some generalized order-disorder transformations. In: Mathematical Proceedings of the Cambridge Philosophical Society. Vol. 48. Cambridge University Press, pp. 106–109.

Raabe, D., 1999. Introduction of a scalable three-dimensional cellular automaton with a probabilistic switching rule for the discrete mesoscale simulation of recrystallization phenomena. Philosophical Magazine A 79 (10), 2339–2358.

Raabe, D., 2002. Cellular automata in materials science with particular reference to recrystallization simulation. Annual review of materials research 32 (1), 53–76.

Read, W. T., Shockley, W., 1950. Dislocation models of crystal grain boundaries. Physical review 78 (3), 275.

Roberts, W., Ahlblom, B., 1978. A nucleation criterion for dynamic recrystallization during hot working. Acta Metallurgica 26 (5), 801–813.

Rollett, A., Luton, M., Srolovitz, D. J., 1992. Microstructural simulation of dynamic recrystallization. Acta Metallurgica et Materialia 40 (1), 43–55.

Rossard, C., Blain, P., 1959. Evolution de la structure de l'acier sous l'effet de la déformation plastique à chaud. Mem. Sci. Rev. Metall 56, 285–300.

Sakai, T., Belyakov, A., Kaibyshev, R., Miura, H., Jonas, J. J., 2014. Dynamic and post-dynamic recrystallization under hot, cold and severe plastic deformation conditions. Progress in Materials Science 60, 130–207.

Schröder, J., Neff, P., Ebbing, V., 2008. Anisotropic polyconvex energies on the basis of crystallographic motivated structural tensors. Journal of the Mechanics and Physics of Solids 56 (12), 3486–3506.

Simo, J. C., 1988. A framework for finite strain elastoplasticity based on maximum plastic dissipation and the multiplicative decomposition: Part I. Continuum formulation. Computer Methods in Applied Mechanics and Engineering 66 (2), 199–219.

Sreekala, S., Haataja, M., 2007. Recrystallization kinetics: A coupled coarse-grained dislocation density and phase-field approach. Physical Review B 76 (9), 094109.

Srolovitz, D., Anderson, M., Grest, G., Sahni, P., 1984a. Computer simulation of grain growth - III. Influence of a particle dispersion. Acta Metallurgica 32 (9), 1429–1438.

Srolovitz, D., Anderson, M. P., Sahni, P. S., Grest, G. S., 1984b. Computer simulation of grain growth - II. Grain size distribution, topology, and local dynamics. Acta Metallurgica 32 (5), 793–802.

Staroselsky, A., Anand, L., 2003. A constitutive model for hcp materials deforming by slip and twinning: Application to magnesium alloy AZ31B. International journal of Plasticity 19 (10), 1843–1864.

Sun, D., Ponga, M., Bhattacharya, K., Ortiz, M., 2017. Proliferation of twinning in hcp metals: Application to magnesium. Journal of the Mechanics and Physics of Solids.

Takaki, T., Hirouchi, T., Hisakuni, Y., Yamanaka, A., Tomita, Y., 2008. Multi-phase-field model to simulate microstructure evolutions during dynamic recrystallization. Materials Transactions 49 (11), 2559–2565.

Tan, J., Tan, M., 2003. Dynamic continuous recrystallization characteristics in two stage deformation of Mg–3Al–1Zn alloy sheet. Materials Science and Engineering: A 339 (1), 124–132.

Totten, G. E., Funatani, K., Xie, L., 2004. Handbook of metallurgical process design. CRC press.

Ulacia, I., Dudamell, N., Gálvez, F., Yi, S., Pérez-Prado, M., Hurtado, I., 2010. Mechanical behavior and microstructural evolution of a Mg AZ31 sheet at dynamic strain rates. Acta Materialia 58 (8), 2988–2998.

Vidyasagar, A., Tan, W., Kochmann, D., 2017. Predicting the effective response of bulk polycrystalline ferroelectric ceramics via improved spectral phase field methods. Journal of the Mechanics and Physics of Solids.

Vidyasagar, A., Tutcuoglu, A. D., Kochmann, D. M., 2018. Deformation patterning in finite-strain crystal plasticity by spectral homogenization with application to magnesium. Computer Methods in Applied Mechanics and Engineering, –In press.
URL https://www.sciencedirect.com/science/article/pii/S0045782518301208

Wang, L., Fang, G., Qian, L., 2018. Modeling of dynamic recrystallization of magnesium alloy using cellular automata considering initial topology of grains. Materials Science and Engineering: A 711, 268–283.

Winning, M., Gottstein, G., Shvindlerman, L., 2001. Stress induced grain boundary motion. Acta materialia 49 (2), 211–219.

Winning, M., Rollett, A. D., 2005. Transition between low and high angle grain boundaries. Acta materialia 53 (10), 2901–2907.

Wolf, D., 1989. A Read-Shockley model for high-angle grain boundaries. Scripta Metallurgica 23 (10), 1713–1718.

Zhang, J., Joshi, S. P., 2012. Phenomenological crystal plasticity modeling and detailed micromechanical investigations of pure magnesium. Journal of the Mechanics and Physics of Solids 60 (5), 945–972.

Zhang, J., Li, W., Guo, Z., 2013. Static recrystallization and grain growth during annealing of an extruded Mg-Zn-Zr-Er magnesium alloy. Journal of Magnesium and Alloys 1 (1), 31 – 38.
URL http://www.sciencedirect.com/science/article/pii/S2213956713000133

Zhao, P., Low, T. S. E., Wang, Y., Niezgoda, S. R., 2016. An integrated full-field model of concurrent plastic deformation and microstructure evolution: Application to 3D simulation of dynamic recrystallization in polycrystalline copper. International Journal of Plasticity 80, 38–55.

Zhao, P., Wang, Y., Niezgoda, S. R., 2018. Microstructural and micromechanical evolution during dynamic recrystallization. International Journal of Plasticity 100, 52–68.